

T-4341

**SOURCE MECHANISM DETERMINATION OF
AFTERSHOCKS OF THE MARCH 9, 1957,
ALEUTIAN ISLANDS EARTHQUAKE**

by

Robert R. Cordray

ARTHUR LAKES LIBRARY
COLORADO SCHOOL OF M
GOLDEN, CO 80401

ProQuest Number: 10783886

All rights reserved

INFORMATION TO ALL USERS

The quality of this reproduction is dependent upon the quality of the copy submitted.

In the unlikely event that the author did not send a complete manuscript and there are missing pages, these will be noted. Also, if material had to be removed, a note will indicate the deletion.



ProQuest 10783886

Published by ProQuest LLC (2018). Copyright of the Dissertation is held by the Author.

All rights reserved.

This work is protected against unauthorized copying under Title 17, United States Code
Microform Edition © ProQuest LLC.

ProQuest LLC.
789 East Eisenhower Parkway
P.O. Box 1346
Ann Arbor, MI 48106 – 1346

T-4341

A thesis submitted to the Faculty and the Board of Trustees of the Colorado School of Mines in Partial fulfillment of the requirements for the degree of Master of Science (Geophysics).

Golden, Colorado

Date 7/29/93

Signed: Robert R. Cordray
Robert R. Cordray

Approved: Thomas M. Boyd
Dr. Thomas M. Boyd

Golden, Colorado

Date July 29, 1993

Phillip Romig
Dr. Phillip Romig
Professor and Head
Department of Geophysics

ABSTRACT

On March 9, 1957, a great earthquake ($M_w=8.6$) ruptured the central Aleutian Arc. Within the rupture zone of the 1957 event, another great earthquake ($M_w=8.0$) occurred on May 7, 1986, much sooner than predicted by recurrence models. Although much is known about the 1986 event, the poor quality of observations of the 1957 event provides little constraint on the mainshock source characteristics. Source mechanisms of its aftershocks, however, do provide valuable information on how slip is accommodated. We determine source mechanisms for eight aftershocks of the 1957 earthquake. For recent events, source mechanisms are determined by inversion of waveforms alone, due to the existence of a well-distributed, well calibrated, seismic network. For the source mechanisms determined here, the lack of well distributed, modelable waveforms requires that P-wave first motions and S-wave polarization directions be used to constrain an a priori fault plane. With this information, the waveforms are inverted for centroid depth, source- time function, and moment, and used as independent confirmation of the a priori strike, dip, and slip. Most of the aftershock mechanisms determined here are similar to those determined in other studies of the Main Thrust Zone and Outer Arc Rise. The one mechanism located along the Unalaska Gap provides inconclusive information on the nature of rupture along that portion of the arc. The two events occurring near Adak Canyon indicate downdip tension in the subducting plate, consistent with previous studies of moment release distribution and fault strength heterogeneities suggesting the MTZ is strongly coupled up dip of their loca-

T-4341

tion, beneath Hawley Ridge. From this, the 1986 event may, in essence, be a large after-shock of the 1957 great earthquake.

TABLE OF CONTENTS

ABSTRACT	iii
LIST OF FIGURES	vii
LIST OF TABLES	xi
ACKNOWLEDGEMENTS	xii
INTRODUCTION	1
Project Overview	5
Method	5
Results	6
BACKGROUND	7
Tectonic Overview	7
Geologic History	7
Arc Geomorphology and Neotectonic Models	8
Seismicity Overview	11
Trench and Outer Arc Rise	12
Main Thrust Zone	13
Overriding Plate	14
Wadati-Benioff Zone	15
METHODOLOGY	17
Available Data	17
P-Wave First Motions	17
S-Wave Polarization Directions	21
Waveform Data	25
Determination and Use of A Priori Constraints	27
Waveform Inversion	31
Solution Error Bounds	35

DISCUSSION	37
Method Effectiveness and Comparison with the Results of Stauder and Udias	38
Tectonic Interpretations	43
Trench and Outer Arc Rise	43
Main Thrust Zone	45
Anomalous Events	47
CONCLUSIONS	49
REFERENCES CITED.	51
APPENDIX.	58
Event 1 March 9, 1957 (20:39:23.92 GMT)	60
Event 2 March 11, 1957 (3:12:48.86 GMT)	62
Event 3 March 11, 1957 (14:55:26.42 GMT)	64
Event 4 March 14, 1957 (14:47:52.09 GMT)	66
Event 5 March 15, 1957 (2:52:16.35 GMT)	68
Event 6 March 22, 1957 (14:21:13.93 GMT).	70
Event 7 April 19, 1957 (14:21:13.93 GMT)	72
Event 8 June 13, 1957 (10:40:46.03 GMT)	74

LIST OF FIGURES

- Figure 1.1: Rupture bounds for the great earthquakes of March 9, 1957 and May 7, 1986. Block boundaries and names are those described by Geist et al. (1988). Triangles indicate active volcanoes (Figure modified from Boyd et al., 1993). 2
- Figure 1.2: Aftershock locations for the great earthquakes of 1957 (left) and 1986 (right). Z57A-D outline regions that showed little seismicity after the 1986 event, but were active after the 1957 event. Likewise, Z86 A-B outline regions of low seismicity for the 1957 event, but higher levels after the 1986 earthquake. Filled circles represent earthquakes with magnitudes above 5.4, open circles are events with magnitudes below 5.4 (modified from Boyd et al., 1993). 3
- Figure 2.1: Schematic diagram of the tectonic history of the Aleutian Arc (from Geist et al., 1988). Explanation of the figure is included in text. 8
- Figure 2.2: Geomorphic and bathymetric map of the central and eastern Aleutian Island Arc. Features important to this study are labeled. Contours are in meters 9
- Figure 2.3: Diagram depicting major elements of the Aleutian subduction zone. Wadati-Benioff zone and trench and outer arc rise events occur within the Pacific plate. Plate boundary earthquakes occur along the main thrust zone, and upper plate seismicity occurs in the shallow region between the seismic and aseismic fronts and beneath the volcanic arc (figure and description from Taber et al., 1991). 12
- Figure 3.1: Lower hemisphere, equal area projection of P-wave first motion data for the March 11, 1957 (3:12:49 GMT) earthquake. The closed circles show compressional first motions. Dilatations are represented by the open circles.. . . . 18
- Figure 3.2: Lower hemisphere, equal area projection of P-wave first motion data for the March 11, 1957 (3:12:49 GMT) earthquake. The data shown has a traveltime residual of one second or less. All symbols are as described in Figure 3.1. 19
- Figure 3.3: P-wave first motion data for the earthquakes of April 19, 1957 (left) and June 13, 1957 (right). All symbols are as described in Figure 3.1. 20
- Figure 3.4: Plot of the direction of horizontal ground motion at the receiver for an arbitrary S-wave. The bold black line represents the ground motion, g_0 is the polarization angle, az is the azimuth of ground motion, and baz is the back azimuth to the epicenter.. . 22
- Figure 3.5: Lower hemisphere, equal area plot of horizontal ground motion at the source for an arbitrary S-wave. Symbols are as defined in Figure 3.4 23
- Figure 3.6: Lower hemisphere, equal area plot of S-wave polarization directions (black lines) for the March 11, 1957 (3:12:49 GMT) earthquake. 24
- Figure 3.7: Lower hemisphere, equal area plot of observed and calculated double couple S-

wave polarization directions for the March 11, 1957 (3:12:49 GMT) earthquake. Calculated directions are shown as gray lines. Observed are black lines. 25
 Figure 3.8: Azimuthal equidistant plot, centered on the epicenter, of stations with available waveform data for the earthquake of 3/11/57 (3:12:49 GMT). The filled black circles represent the station locations. Circular arcs are spaced at 45° increments. 27
 Figure 3.9: Lower hemisphere projection of observed P-wave first motion and S-wave polarization data for the earthquake of March 11, 1957 (3:12:49 GMT). The curved black lines represent P-wave nodal planes. All other symbols are as described in Figure 3.1 and Figure 3.6. 28
 Figure 3.10: Percent-likelihood regions for the *P* (left) and *T* (right) axes positions for the earthquake of 3/11/57 (3:12:49 GMT). The entirely black region contains solutions which comprise 95% of the total likelihood. The grayscale includes extensions up to 99% of the total likelihood. 32
 Figure 3.11: Average *P* and *T* axes solution for the earthquake of 3/11/57 (3:12:49 GMT). All symbols are as described in Figure 3.7. 33
 Figure 3.12: Waveform solution for the earthquake of 3/11/57 (3:12:49 GMT). Station name abbreviations are given in Table 3.1. Amplitude (normalized to an instrument 60° from the source with a gain of 3000) and time scale is shown in the lower right hand corner. 35
 Figure 4.1: Source mechanisms as determined by Stauder and Udias (1963). 400 m bathymetry contours border the arc and 6000 m contours border the trench. Epicenter locations are from Boyd et al.(1993). Source mechanisms are lower hemisphere projections, with shaded compressional quadrants. Event numbers correspond to Table 4.1. 39
 Figure 4.2: Results of Stauder and Udias (left) and this study (right) for the Group I earthquake of 3/11/57 (14:55:26.42 GMT). Included is the relative value of R_{ps} for each solution. All symbols are as described in Figure 3.9. 40
 Figure 4.3: Results of Stauder and Udias (left) and this study (right) for the earthquakes of their Group I variant. All symbols are as described in Figure 3.9. 42
 Figure 4.4: Source mechanisms determined in this study. All symbols are as described in Figure 4.1. 44
 Figure 4.5: Cross sectional view of seismicity of the Adak Island region from the study of Ekström and Engdahl (1989). Events 2, 3, 4, and 8 are the striped circles labeled in the figure. The grid spacing is 50 km. The relocated hypocenters and locations of the volcanoes are rotated into a plane locally perpendicular to the arc (Figure modified from Ekström and Engdahl, 1989). 45
 Figure 4.6: (left) Depth of events 1, 5, 6, and 7 relative to the depths recorded by the Unalaska seismic network. The mechanism is a back hemisphere projection in the plane of the cross section indicated by XX' in the map on the right (modified from Boyd and Jacob, 1986).. 46
 Figure A.1 Epicenter locations and source mechanisms of modeled events. Map is based on an Albert's projection. Source mechanisms are indicated on lower hemisphere, equal

area projections with shaded compressional quadrants. Event numbers refer to Table A-1. 58

Figure A.2: *P* and *T* axes error surfaces for the earthquake of 3/9/57 (20:39:23.92 GMT). Symbols are as described in Figure 3.10. 60

Figure A.3: Waveform solutions for for the earthquake of 3/9/57 (20:39:23.92 GMT). Location of station recording the S-waves (HON) is shown for reference. 61

Figure A.4: First motion and S-wave polarization data for for the earthquake of 3/9/57 (20:39:23.92 GMT).. 61

Figure A.5: *P* and *T* axes error surfaces for the earthquake of 3/11/57 (3:12:48.86 GMT). Symbols are as described in Figure 3.10. 62

Figure A.6: Waveform solutions for the earthquake of 3/11/57 (3:12:48.86 GMT). . . 63

Figure A.7: First motion and S-wave polarization data for the earthquake of 3/11/57 (3:12:48.86 GMT). 63

Figure A.8: *P* and *T* axes error surfaces for the earthquake of 3/11/57 (14:55:26.42 GMT). 64

Figure A.9: Waveform solutions for the earthquake of 3/11/57 (14:55:26.42 GMT) . . 65

Figure A.10: First motion and S-wave polarization data for the earthquake of 3/11/57 (14:55:26.42 GMT) 65

Figure A.11: *P* and *T* axes error surfaces for the earthquake of 3/14/57 (14:47:52.09 GMT) 66

Figure A.12: Waveform solutions for the earthquake of 3/14/57 (14:47:52.09 GMT) . 67

Figure A.13: First motion and S-wave polarization data for the earthquake of 3/14/57 (14:47:52.09 GMT) 67

Figure A.14: *P* and *T* axes error surfaces for the earthquake of 3/15/57 (2:52:16.35 GMT) 68

Figure A.15: Waveform solutions for the earthquake of 3/15/57 (2:52:16.35 GMT) . . 69

Figure A.16: First motion and S-wave polarization data for the earthquake of 3/15/57 (2:52:16.35 GMT). 69

Figure A.17: *P* and *T* axes error surfaces for the earthquake of 3/22/57 (14:21:13.93 GMT) 70

Figure A.18: Waveform solutions for the earthquake of 3/22/57 (14:21:13.93 GMT) . 71

Figure A.19: First motion and S-wave polarization data for the earthquake of 3/22/57 (14:21:13.93 GMT) 71

Figure A.20: *P* and *T* axes error surfaces for the earthquake of 4/19/57 (14:21:13.93 GMT) 72

Figure A.21: Waveform solutions for the earthquake of 4/19/57 (14:21:13.93 GMT) . 73

Figure A.22: First motion and S-wave polarization data for the earthquake of 4/19/57 (14:21:13.93 GMT) 73

Figure A.23: *P* and *T* axes error surfaces for the earthquake of 6/13/57 (10:40:46.03 GMT) 74

Figure A.24: Waveform solutions for the earthquake of 6/13/57 (10:40:46.03 GMT) . 75

Figure A.25: First motion and S-wave polarization data for the earthquake of 6/13/57
(10:40:46.03 GMT) 75

LIST OF TABLES

Table 3.1: Stations used in this study 26

Table 3.2: Instrument Parameters 34

Table 4.1: Event Locations and Origin Times 37

Table A.1: Event Locations and Origin Times. 59

ACKNOWLEDGEMENTS

I would like to thank Dr. Tom Boyd for his assistance and, most importantly, his patience during the preparation of this thesis. Our frequent discussions (scientific and not so scientific), soccer matches, alpine research trips, lunches, and watching of hair washings were most enjoyable. His suggestion of me attending field camp is also appreciated as the one act that has changed and complicated my life in ways I never thought possible. Fun is most definitely conserved.

For the remainder of my M. S. committee, thanks to Dr. Frank Hadsell for the shocking baptism into Mines (GP 501) and assistance with Framemaker. Additional thanks to the Jefferson County court system, whose jury selection criteria substituting my trial for one of their's was a welcome relief, lest Dr. Hadsell be replaced by faculty whose name can be maliciously conjugated. Also, thanks to Dr. Ron Knoshaug for GP 404 and wonderful biting social commentary during the Lake George portion of field camp. A picture is worth a thousand words, but a good rolling of the eyes speaks volumes.

This thesis would have not been nearly as enjoyable (nor taken as long to produce) without the wonderful friends and places I have acquainted during my stay. Thanks and farewell to the mountains, the Oyster Club, the Mesa, the Ace, Lane's Tavern, the field camp crew, Dave "dad patrol" Lane, Terry "your nickname for me will get me in trouble" Nichols, Will "huh?" Barnard, Nick "I'm in a band" White, Rob "let's go to jail" Kendall, Gary "I'm not negative" Elkington, Earl "can you watch my dogs?" Williams, Craig "you

are a dog” Artley, Yaroslav “the smiling Czech” Chronac, Timo “Rob, you made me drink again” Tjan, Asbjorn “so eloquently put, Rob” Christensen, Carl “I don’t complain” Lackner, “Ri”, and PootenAndy.

On a more serious note, no one deserves more credit for my completion of this degree than my mother, Mary E. Cordray. We went through some difficult times together, most of them being my fault, but she never gave up on me (I’m sure she thought about it). Her unfortunate reward is me taking a job where I’ll rarely see her. Of course, I guess that’s better than me taking a job at Conrad’s and moving back in.

This work was supported by USGS NEHRP program grant 14-08-0001-G1766 and a grant from DuPont.

CHAPTER 1

INTRODUCTION

The aftershock zone of the great Aleutian earthquake of March 9, 1957 ($M_w=8.6$) covered a 1200-km long segment of the arc (Sykes, 1971). Twenty-nine years later, on May 7, 1986 ($M_w=8.0$), another great event nucleated near the epicenter of the 1957 event and reruptured a 250-km long section of the arc. This second event was unexpected, since, assuming an arc wide average recurrence interval (e.g. Jacob, 1984), the probability of great earthquake rerupturing the 1957 rupture zone appeared to be quite low (<10%).

Several studies (e.g. Ekström and Engdahl, 1989; Boyd and Nabelek, 1988; Das and Kostrov, 1990) have investigated the moment release, aftershock source mechanisms, and seismicity precursory to the 1986 event. This earthquake nucleated 44 km to the west of the epicenter of the 1957 event (Figure 1.1) and ruptured bilaterally, with most of the moment release concentrated 40 to 80 km west of the epicenter along the upper plane of the Main Thrust Zone (MTZ). Less moment originated east of the epicenter, along the lower plane. Houston and Engdahl (1989) found that seismicity west of the epicenter occurred in both the upper and lower plane of the MTZ, but was confined to the upper plane in the eastern rupture zone, anti-correlated with the distribution of moment release.

Although much is known about the 1986 earthquake, source characteristics of the 1957 event are not well constrained. Estimates of the size of the source region based on tsunami studies (e.g. Satake and Johnson, 1992) and surface wave directivity studies

(Lane, 1992) indicate coseismic slip did not occur along the easternmost 150 kms of the aftershock zone, although neither study resolves the westward rupture bounds to better than 1° of longitude. Moment release distribution is similarly unresolved, with most estimates assigning the largest moment release to the westernmost 600 km of the aftershock zone (Ruff et al., 1986) and a small high-moment release area around 170° W (Satake and Johnson, 1992). House et al. (1981) refer to the easternmost portion of the aftershock zone as the Unalaska Seismic Gap and suggest that it may be the site of a future great earthquake. Given the quality of seismograms of the mainshock and the broad spatial extent of

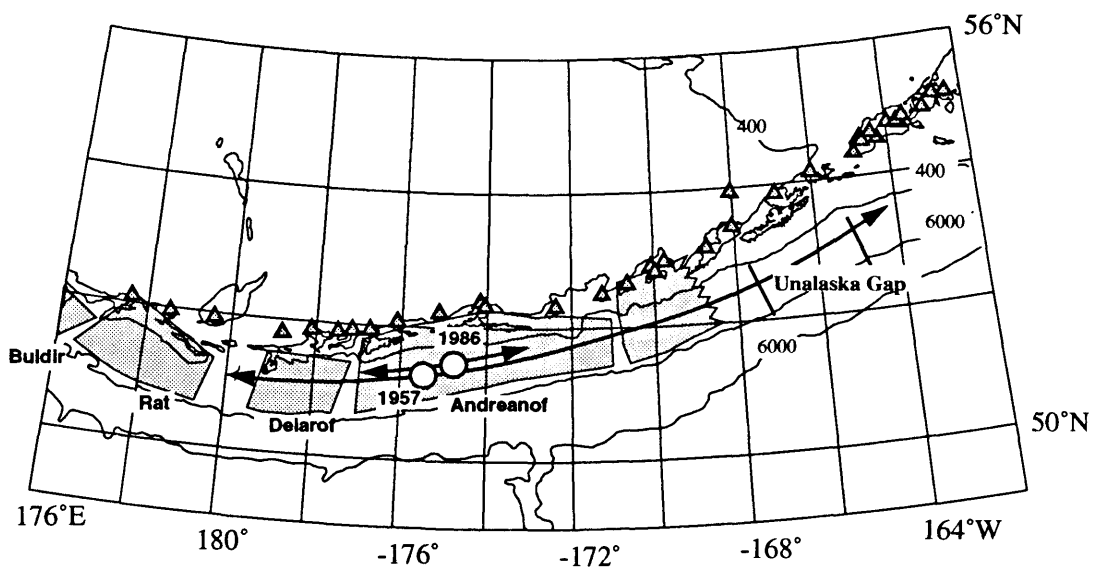


Figure 1.1: Rupture bounds for the great earthquakes of March 9, 1957 and May 7, 1986. Block boundaries and names are those described by Geist et al. (1988). Triangles indicate active volcanoes (Figure modified from Boyd et al., 1993).

current source estimates, it is unlikely that a more detailed picture of the source character-

istics is forthcoming.

In an effort to better resolve the 1957 mainshock and understand the short interseismic period, Boyd et al. (1993) cataloged and relocated seismicity along the central Aleutian Arc occurring between 1957 and 1989. These relocations are based on P-wave arrival times published in the ISS (International Seismological Summary), BCIS (Bulletin Mensuel de Bureau Central International de Seismologie), and ISC (International Seismological Centre) bulletins. Corrections are made to the travel times for near source velocity anomalies associated with the subducting slab.

One of the results of this relocation study is the apparent anticorrelation in the aftershock sequences of the 1957 and 1986 great earthquakes (Figure 1.2). Zones which

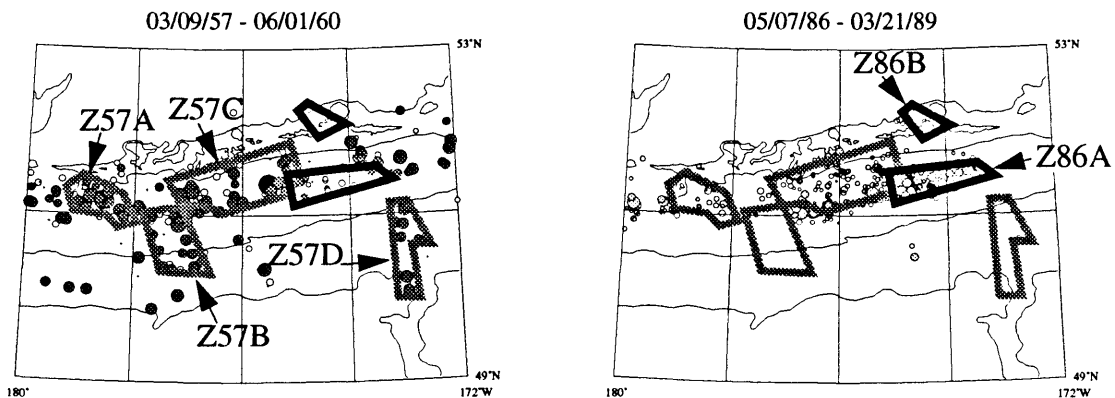


Figure 1.2: Aftershock locations for the great earthquakes of 1957 (left) and 1986 (right). Z57A-D outline regions that showed little seismicity after the 1986 event, but were active after the 1957 event. Likewise, Z86 A-B outline regions of low seismicity for the 1957 event, but higher levels after the 1986 earthquake. Filled circles represent earthquakes with magnitudes above 5.4, open circles are events with magnitudes below 5.4 (modified from Boyd et al., 1993).

had high rates of seismicity (magnitudes > 5.4) during the 1957 aftershock sequence (Z57A, Delarof Block; Z57B, near Adak Canyon; Z57D, trench west of Amlia Fracture Zone) showed little seismicity following the 1986 earthquake. Similarly, aftershocks of the 1986 earthquake were confined to the eastern edge of the mainshock rupture zone (Z86A) with some events in the backarc north of Andreanof Island (Z86B).

In addition to the spatial relationships of the aftershock sequences, source mechanisms provide valuable information about how slip is accommodated. Preliminary analysis of the rupture processes of the 1957 event (Lane, 1992) and of the 1986 event (Ekström and Engdahl, 1989) indicate the rupture bounds and aftershock sequences are controlled by mappable geologic features in the overriding plate. Models of overriding plate deformation (Geist et al., 1988) suggest strong coupling of certain sections (Figure 1.1) of the overriding plate to the subducting Pacific plate. This model has been supported by source mechanisms determined for the 1986 earthquake (Ekström and Engdahl, 1989) and the interseismic period (e.g. Stauder, 1968; House, 1983), but not for the 1957 event.

We estimate source mechanisms of as many aftershocks of the 1957 event as possible. Given the limited amount of data available, these aftershocks provide one of the few available constraints on the mainshock rupture process. Although difficulties are expected with the historic data, a better understanding of the slip accommodated during this great event may help us understand the short interseismic period and the control of the overriding plate on shallow seismicity in the central Aleutian arc.

Project Overview

Determining source mechanisms from historic data is no small task. For recently recorded earthquakes, quick and accurate determination of source mechanisms is possible because there is a well-distributed, well calibrated, seismic network. Unfortunately, for events recorded prior to 1964, this analysis is hampered by the sparsity of quality data recorded on instruments with known responses. Modern techniques, based on the inversion of waveform data alone, are difficult to directly apply to these historic observations. By combining methods and datasets utilized by previous researchers (e.g. Stauder and Udias, 1963; Dillinger et al., 1971; Nabelek, 1984), however, well constrained source mechanisms can be determined.

Method

We analyze P-wave first motion directions (from various catalogues), S-wave polarization directions (Stauder and Udias, 1963), and microfilmed earthquake records (Glover, 1985) as a means of constraining source mechanisms for several aftershocks of the March 9, 1957 Aleutian Islands earthquake. Using the first two data sets, previous studies used “trial and error” graphical methods (e.g. Stauder and Udias, 1963) for source mechanism determination. This study constructs maximum likelihood regions (Dillinger et al., 1971) for *P* and *T* axes from the P-wave first motions and S-wave polarization directions, constraining the strike, dip, and slip of the solution. The mathematical nature of this method reduces researcher bias that can accompany graphical methods, as the only ad-hoc constraints for the likelihood determination are the estimated measurement errors in the P-

and S-wave data.

Because of the limited azimuthal distribution of the waveform data, the inversion is unstable, and, without a priori information, convergence is nearly impossible. We use the P and T axes bounds as soft a priori constraints on fault strike, dip, and slip, and invert the waveform data for centroid depth, seismic moment, and source time function. In the absence of SH-waveforms, convergence requires the a priori strike, dip, and slip to be held constant. The inversion is then carried out for centroid depth, seismic moment, and source time function. From this, the final solution is chosen to be the source mechanism that best fits all of the available datasets.

Results

In this thesis, we determine source mechanisms for eight aftershocks of the 1957 great earthquake. Several of the aftershock source mechanisms are similar to those proposed by previous researchers (e.g. Ekström and Engdahl, 1989; House and Jacob, 1983) for the MTZ and the Outer Arc Rise. Little insight is provided by the one source mechanism determined for the Unalaska Gap. Two events occurring near Adak Canyon suggest downdip tension in the subducting plate, consistent with the MTZ being strongly coupled beneath Hawley Ridge and remaining unruptured during the 1957 event. This conclusion is also supported by the moment release distribution inferred from aftershock relocations (Boyd et al., 1993) and the fault strength heterogeneities from geologic observations (Ryan and Scholl, 1993).

CHAPTER 2

BACKGROUND

Tectonic Overview

Geologic History

Referring to Figure 2.1 (from Geist et al., 1988), the geologic history of the arc began at about 55 Ma, when subduction ceased at the Berinigan margin and began at the Aleutian arc. With subduction rates as high as 200 km/my, rapid magma generation created most of the arc by middle Eocene time. At 43 Ma, a change in the motion of the Pacific plate (the same which created the bend in the Emperor seamount chain) resulted in a decrease in subduction rate, to approximately 58-70 km/my. This coincided with the abandonment of the Kula Ridge and subsequent emergence and plutonism of the arc due to subduction of the younger Kula plate. At 10 Ma, subduction of the dead Kula ridge initiated subsidence of the arc, due to subduction of the increasingly older lithosphere. 5 Ma marked a slight increase in the northerly azimuth and rate of subduction, consequently increasing volcanic activity, forearc turbidite sedimentation, and forming the subduction complex.

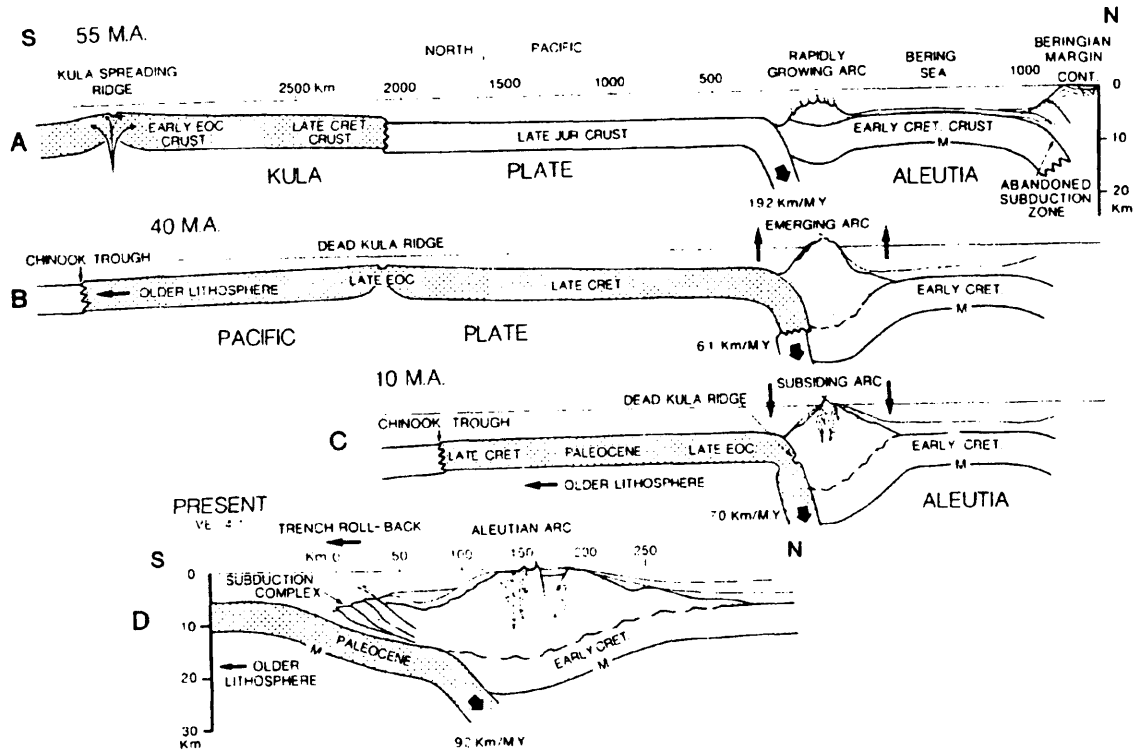


Figure 2.1: Schematic diagram of the tectonic history of the Aleutian Arc (from Geist et al., 1988). Explanation of the figure is included in text.

Arc Geomorphology and Neotectonic Models

Referring to Figure 2.2, the central Aleutians is dominated by three main geomorphic features: the summit platform of the Aleutian Arc, the Aleutian Terrace, a forearc basin at about 5 km water depth, and the lower, landward slope of the Aleutian Trench from 5 to 7-km water depth (Ryan and Scholl, 1993). The forearc is typical of convergent plate margins and consists of an accretionary wedge, an outer arc high, and a forearc

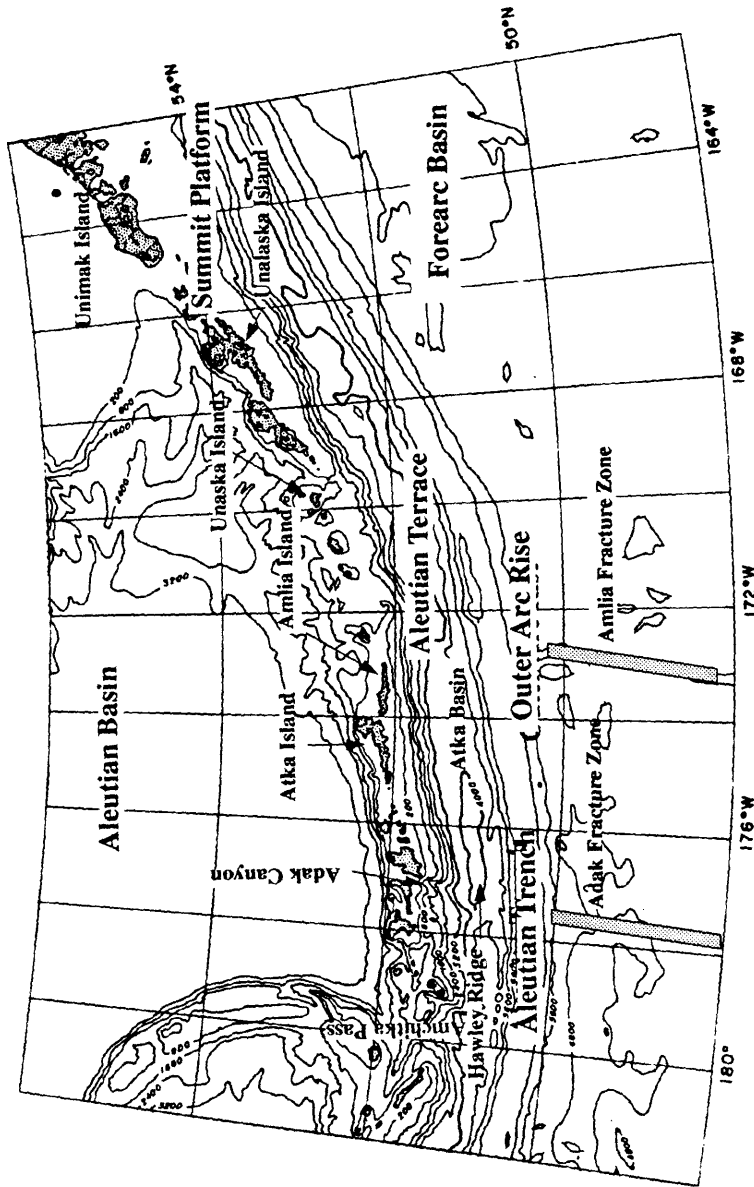


Figure 2.2: Geomorphic and bathymetric map of the central and eastern Aleutian Island Arc. Features important to this study are labeled. Contours are in meters

basin. An outer arc high called Hawley Ridge (located between 175° W and 177° W on the Aleutian Terrace) is bounded to the south by a major right lateral shear zone (Ryan and Scholl, 1989). Uplift beneath Hawley Ridge, presumably caused by along-arc transport of basement rocks, may cause an increase in interplate coupling (Ekström and Engdahl, 1989).

Along the central Aleutians, the subducting Pacific plate contains two fracture zones, the Amlia fracture zone (north south axis trends at about 173.1° W) and the Adak fracture zone (north south axis trends at about 177.4° W). The Amlia fracture zone has a left lateral offset of approximately 220 km (Grim and Erickson, 1969) and is a mappable feature in the subducting plate from at least 45° N to where it intersects the trench. At the intersection, an offset in the trends of deep seismicity and the volcanic arc suggest the downgoing plate is offset at depth by about 40 km in a right lateral sense (House and Jacob, 1983). The Adak fracture zone is less striking than the Amlia Fracture Zone, with a left lateral offset of about 30 km. The point at which this fracture intersects the trench coincides with several discontinuities in the overriding plate, but any association is probably circumstantial (Ekström and Engdahl, 1989).

The summit platform of the central Aleutian arc is divided by three submarine canyons: Amchitka Pass (180°), Adak Canyon (177° W), and a broad canyon south of Yunaska Island (171° W). As early as 1956, Gates and Gibson proposed that these canyons are of tectonic, rather than erosional origin. In addition to the canyons, this region contains many intra arc “summit” basins, of which several are located near the arcward extension of the aforementioned fracture zones.

Models proposed to explain these and other features of the arc range from the location of ascending or descending magmatic fronts to the spreading of fracture zones during subduction (Taber et al., 1991). These models, however, could not explain the occurrence of all the canyons and summit basins.

A more inclusive model was proposed by Geist et al. (1988). In their model, the overriding plate is broken into several distinct blocks (Figure 1.1), each rotating clockwise and translating westward, in response to the oblique direction of subduction. The blocks are distributed along the arc from about 170° W, where subduction is nearly perpendicular to the arc, to 170° E, where the subduction parallels the arc. In this model the transverse canyons represent left lateral shear zones between blocks, and the summit basins are tear structures formed in the wake of clockwise rotating blocks. Arc parallel shear zones form the northern and southern boundaries of each block. The individual blocks appear to be strongly coupled to the downgoing plate, and less coupled to one another (Geist et al., 1988). Most important to this study, the block boundaries seem to coincide with and perhaps control the rupture bounds of the great earthquakes (Taber et al., 1991, Ryan and Scholl, 1993).

Seismicity Overview

Seismicity of the Aleutian Island chain can be divided into four distinct regions: the trench and outer arc rise, the main thrust zone, the upper plate, and the Wadati-Benioff zone (Figure 2.3).

Trench and Outer Arc Rise

Fewer earthquakes occur in the trench and outer arc rise than in the rest of the Aleutian Arc. Information from an ocean bottom seismometer study of the central Aleutians (Frohlich, et. al., 1982) is probably representative of much of the arc (Taber et al.,

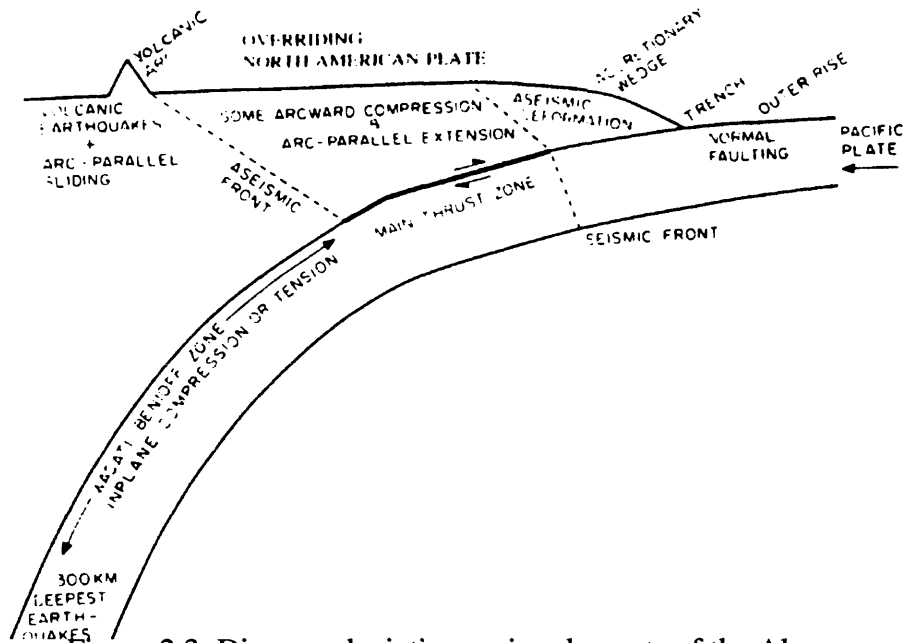


Figure 2.3: Diagram depicting major elements of the Aleutian subduction zone. Wadati-Benioff zone and trench and outer arc rise events occur within the Pacific plate. Plate boundary earthquakes occur along the main thrust zone, and upper plate seismicity occurs in the shallow region between the seismic and aseismic fronts and beneath the volcanic arc (figure and description from Taber et al., 1991).

1991). This study indicates that events in the trench and outer arc rise are less than 20 km deep, and occur in a zone 10 km landward and 60 km oceanward of the trench. Most

events are normal faulting, presumably caused by tensile stresses induced in the Pacific plate as it bends beneath the Aleutian arc. Evidence exists that these earthquakes may be related to great events occurring along the main thrust zone, as the compressional stress release on the plate interface causes the outer arc portion of the subducting plate to be placed in tension (Spence, 1987). Outer arc compressional events have occurred in other subduction zones before great thrust earthquakes (Christensen and Ruff, 1983), but none have been observed in the Aleutians.

Main Thrust Zone

The great earthquakes which release most of the accumulated strain in the arc occur along the main thrust zone (MTZ). The MTZ dips most steeply (25° to 30°) in the central Aleutians, coinciding with the smallest volcanic arc-trench separation (170 km). Seismic coupling with the overriding plate does not occur trenchward of the seismic front (Figure 2.3), probably because unconsolidated sediments in the accretionary wedge lack the strength to support earthquakes. Along -arc variations in the arc-trench separation appears to be due to almost entirely to an increase in the width of the accretionary wedge (Jacob, 1977). The aseismic front occurs in a similar location along most subduction zones (Taber et al., 1991), and marks the arcward limit of MTZ seismicity. Seismic coupling along the MTZ has been attributed to seaward advance of the back arc plate, resistance to bending of the subducting plate, and many other factors (Spence, 1987).

Most earthquakes located along the MTZ occur on low angle thrust faults with slip directions oriented northwest of the normal to the trend of the trench (e.g. Ekström and

Engdahl, 1989). Stauder (1972) found that MTZ seismicity within the blocks appears, at least temporarily, to be independent of events in neighboring blocks. Sudden changes in the stress field of the Rat block appeared to have little effect on the events in the Delarof or Andeanof blocks, and vice versa. Ekström and Engdahl (1989) and House and Jacob (1983) found several mechanisms along the MTZ that show along arc tension, presumably caused by westward extension of the overriding plate.

Overriding Plate

Seismicity levels in the overriding plate are less than those in the main thrust zone, but greater than those in the Trench and Outer Arc Rise. For events recorded by the Shumagin Island network, Reyners and Coles (1982) found mostly horizontal compression parallel to the direction of convergence, indicating stress transfer across the plate interface to the overlying plate. Stauder (1968) observed a strike slip event between the Delarof and Rat blocks concurrent with the limits of the aftershock zone of the great 1965 Rat Islands earthquake, indicating arc-arc transform faulting like that of Geist et al. (1988). Aftershock studies of the 1986 event by Ekström and Engdahl (1989) found several strike slip mechanisms located to the north of Atka Island. Boyd and Nabelek (1988) estimated their source depths to be less than 15 km, placing them in the overriding plate. Analysis of the aftershocks of these events indicate right lateral strike-slip movement, along an arc parallel fault system, suggesting decoupling of the slip into two distinct zones, as suggested by Geist et al. Ekström and Engdahl, based on worldwide plate motion models, estimate up to 3 cm/yr of slip may be accommodated by this fault system. Since the relative plate conver-

gence direction is only 35° from the normal to the trend of the trench, this fault would have low shear strength. Boyd and Nabelek (1988) point out, however, that the left lateral solution of the other nodal plane is also plausible, and could indicate the rebound of the overlying plate after the 1986 earthquake.

Wadati-Benioff Zone

Most events in this zone are intraplate downdip compressional and tensional earthquakes, and occur at a smaller and more uniform rate than those along the main thrust zone (Taber et al., 1991). There is a transition zone of low seismicity between the MTZ and the Wadati-Benioff Zone, as earthquakes change from shallow interplate events to intraplate events at depth (Ekström and Engdahl, 1989). The Wadati-Benioff Zone dips between 30° in the Shumagin Island region to 60° in the Adak region, with teleseismic focal mechanisms indicating downdip tension in the eastern Aleutians and downdip compressions in the western Aleutians (Taber et al., 1991). The dip variations are accompanied by changes in the maximum depth of seismicity, with the cutoff occurring at depths of more than 250 km in the central and eastern portions of the arc and less than 50 km in the western Aleutians. The maximum depth of seismicity is concurrent with an isotherm in the kinematic flow model of Creager and Boyd (1991), suggesting earthquakes terminate because of the initiation of high temperature, steady-state creep. The maximum depth of seismicity in the Aleutians is less than other subduction zones because of the relative youth of the subducting plate (Figure 2.1).

The geometry of the subducting plate has been determined by event relocation

studies that include the heterogeneous velocity structure of the subducting slab (e.g. Engdahl and Gubbins, 1987). This study indicates a slab thickness of 80 to 100 km and a downdip depth of about 400 km, although seismic activity ceases below 250 km. Boyd and Creager (1991) found a slab depth of 600 km better fit travel times of P-waves for earthquakes located along the central Aleutians. Their study also implied the existence of subducted lithosphere 300 km beneath the seismicity cutoff along the entire arc. This is most surprising in the western Aleutians, where previous studies refuted the existence of a slab because of the direction of relative plate motion, the lack of deep seismicity, and the lack of Holocene volcanism (e.g. Newberry, 1986; Lonsdale, 1988).

CHAPTER 3

METHODOLOGY

Because of the limited amount, and the dubious quality of information in a single historical dataset, several different sources are necessary to determine accurate source mechanisms. For this reason, methods used on better recorded, more recent earthquakes are, in general, not applicable. This study uses three datasets for a joint determination of seismic moment, centroid depth, source-time function, and fault plane strike, dip, and slip. Strike, dip, and slip along the fault plane are initially constrained by P-wave first motions and S-wave polarization directions. P and SH waveform data are then used to constrain centroid depth and seismic moment, and refine estimates of strike, dip, and slip.

Available Data

P-Wave First Motions

The P-wave first motion data gathered at each station are tabulated in the ISS (International Seismological Summary, 1957). We display P-wave first motion data, as is routinely done, by plotting them on a lower hemisphere, equal area projection centered at the source. As an example, Figure 3.1 shows the P-wave first motion data for an earthquake that occurred on March 11, 1957 (3:12:49 GMT). Filled circles indicate compressional first arrivals while open circles dilatational first arrivals.

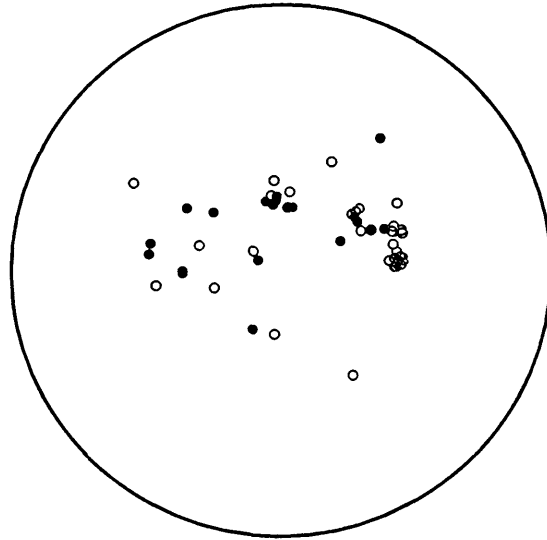


Figure 3.1: Lower hemisphere, equal area projection of P-wave first motion data for the March 11, 1957 (3:12:49 GMT) earthquake. The closed circles show compressional first motions. Dilatations are represented by the open circles.

There are several problems inherent in this dataset, resulting in it being rather inconsistent. First, polarities were commonly determined from short period records, which are typically noisy, making it difficult to pick first motions correctly. Second, the phase whose polarity was reported may not be the P-wave, but rather one of the depth phases, pP or sP. This can happen near P-wave nodal planes, where pP or sP may be much larger on the seismogram than P. Although the problem may be corrected by comparing different seismograms generated by the same earthquake, individual operators responsible for seismogram interpretation and reporting to the ISS cannot do this. Third, the polarity of the instrument may be incorrect, resulting in reports opposite of the actual arrival. Finally, first

arrivals may be very emergent, because stations are located near nodal planes or because of a slow rupture process.

The phase identification problem is minimized by not using first motions associated with more than a one second traveltime residual with respect to a slab corrected velocity model (Boyd et al., 1993). Unfortunately, although more consistent, applying this residual cutoff for the March 11, 1957 (3:12:49 GMT) earthquake still results in P-wave first motion data that is too sparse to determine the source mechanism (Figure 3.2). Simi-

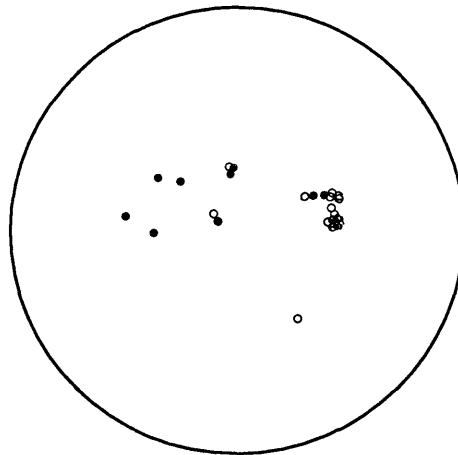


Figure 3.2: Lower hemisphere, equal area projection of P-wave first motion data for the March 11, 1957 (3:12:49 GMT) earthquake. The data shown has a traveltime residual of one second or less. All symbols are as described in Figure 3.1.

lar filtering for the April 19, 1957 and June 13, 1957 events (Figure 3.3) gives the same results. Despite these difficulties, P-wave first motions represent a useful and important dataset.

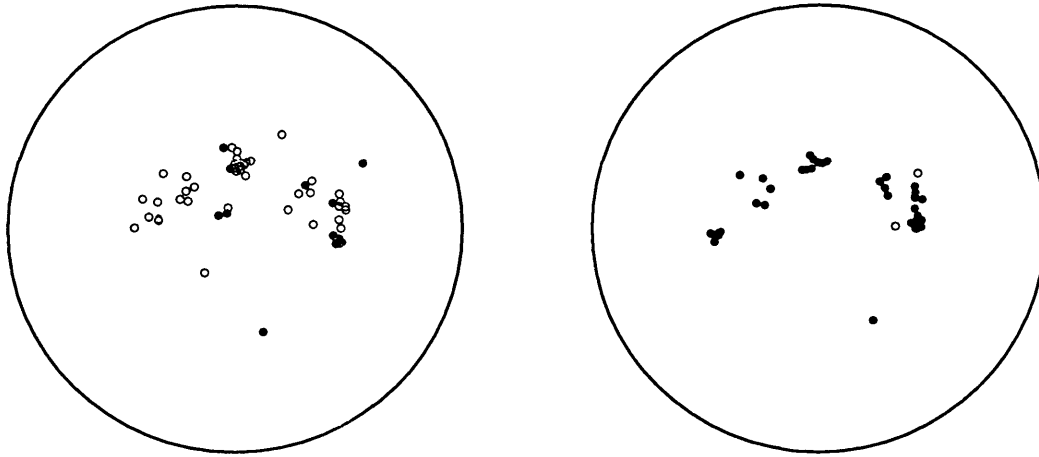


Figure 3.3: P-wave first motion data for the earthquakes of April 19, 1957 (left) and June 13, 1957 (right). All symbols are as described in Figure 3.1.

For example, of the two events shown in Figure 3.3, it is clear that the first motions of the 4/19/57 event are dominated by dilatations while those of 6/13/57 are dominated by compressions. From this observation we conclude that the event of 4/19/57 is normal faulting, while that of 6/13/57 is thrust faulting. We cannot conclude, however, by this data alone, the orientations of the fault planes for these two events. Likewise, for the event of March 11, 1957 (3:12:49 GMT) (Figure 3.2), we observe dominately compressional first arrivals, but there is a coherent patch of dilatational arrivals observed due east of the epicenter. Although this could be consistent with a thrust faulting event, it is unusual to observe such a coherent group of dilatational arrivals in this location. More typically we would observe inconsistent first motions in this portion of the focal sphere, indicative of a nodal plane crossing (see, for example, Figure A.16). In this way, we use the first motion

data to classify events into one of three source types: thrust faulting, normal faulting, or events with coherent first motions not consistent with thrust or normal faulting.

S-Wave Polarization Directions

S-wave polarization directions for the aftershocks were determined by Stauder and Udias (1963). The S-Wave Project was designed to graphically determine source mechanisms of the larger earthquakes each year using P- and S-wave information from microfilm files of the recording stations. This particular report was part of a study of earthquakes of the North Pacific, and includes source parameters for 25 Aleutian Island earthquakes, 17 of which were aftershocks of the 1957 earthquake.

S-wave polarization directions are determined by plotting a hodogram of the horizontal S-wave ground motion from the N-S and E-W records. This direction of horizontal ground motion is then plotted at the receiver as shown in Figure 3.4. To simplify the analysis, the S-wave ground motion is resolved into radial (SV) and tangential (SH) components. The polarization angle is then defined as

$$\gamma_o = \tan^{-1} \left(\frac{SH}{SV} \right), \quad \text{EQ 3.1}$$

that is, the arc tangent of the ratio of the SH amplitude to the horizontal SV amplitude (Stauder and Bollinger, 1964). An incoming wave that is pure SV has all of its horizontal ground motion parallel to the back azimuth direction, hence its polarization angle is 0° . Similarly, pure SH motion would be perpendicular to the back azimuth direction, resulting in a polarization angle of 90° . γ_o is defined as positive for counterclockwise acute angles

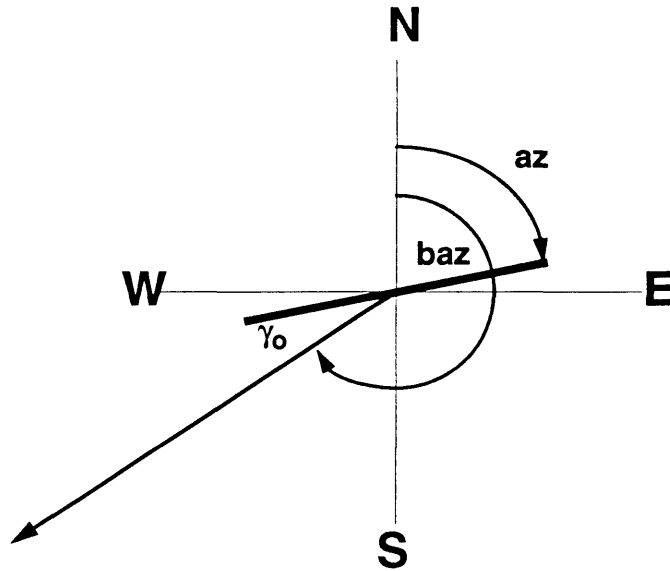


Figure 3.4: Plot of the direction of horizontal ground motion at the receiver for an arbitrary S-wave. The bold black line represents the ground motion, γ_0 is the polarization angle, az is the azimuth of ground motion, and baz is the back azimuth to the epicenter.

looking from the source to the station (clockwise acute angles are negative).

After calculating S-wave polarization directions for each station, the data is plotted on a lower hemisphere, equal area projection, usually with the P-wave first motion information. Figure 3.5 shows the projection for a single station, where az is now the azimuth to the station and toa is the takeoff angle of the observed S-wave. Because the projection is lower hemisphere, γ_0 is positive in the clockwise direction, looking from the source to the station.

As an example, Figure 3.6 shows the polarization data for the event of March 11,

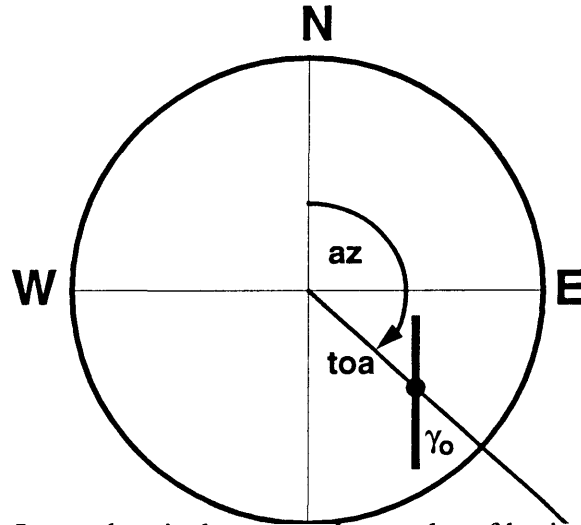


Figure 3.5: Lower hemisphere, equal area plot of horizontal ground motion at the source for an arbitrary S-wave. Symbols are as defined in Figure 3.4

1957 (3:12:49 GMT). Only data from stations located between 44° and 80° epicentral distance are included from the dataset of Stauder and Udias. For distances less than this range, post-critically reflected SV waves are phase shifted relative to the SH, making the graphical determination of the polarization direction incorrect. Also, the short distance rays have much of their travel path in the shallow mantle, making distinguishing between S and S_n difficult. For the longer distances, interference from the core phases make separation of the S-wave from SKS, ScS, SP, or SKKS impossible. These and other problems associated with the selection of range of acceptable distances are discussed in greater detail in Stauder and Bollinger (1964).

For a given double couple solution (Aki and Richards, 1980), takeoff angle, azi-

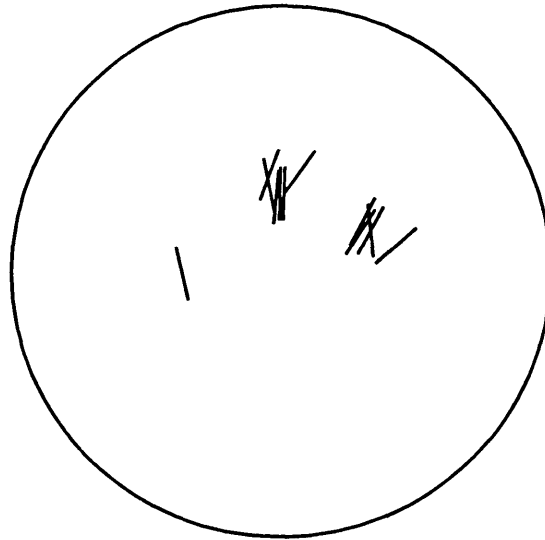


Figure 3.6: Lower hemisphere, equal area plot of S-wave polarization directions (black lines) for the March 11, 1957 (3:12:49 GMT) earthquake.

ment, and the S-wave polarization directions are easily calculated. We plot the computed polarization directions as gray line segments of a lower hemisphere, equal area projection. Figure 3.7 shows the observed data with polarization angles, calculated assuming a fault orientation consistent with a typical thrust faulting earthquake along the MTZ (e.g. Ekström and Engdahl, 1989), for the earthquake of March 11, 1957 (3:12:49 GMT).

As suggested by the P-wave data, notice that the S-wave polarizations are also inconsistent with a thrust faulting event along the MTZ. This dataset alone, like P-wave first motions, is not enough to uniquely constrain the source mechanism. For example, S-wave polarization observations contain no information on polarity, therefore, it is impossible to distinguish between thrust and normal faulting earthquakes. The S-wave polariza-

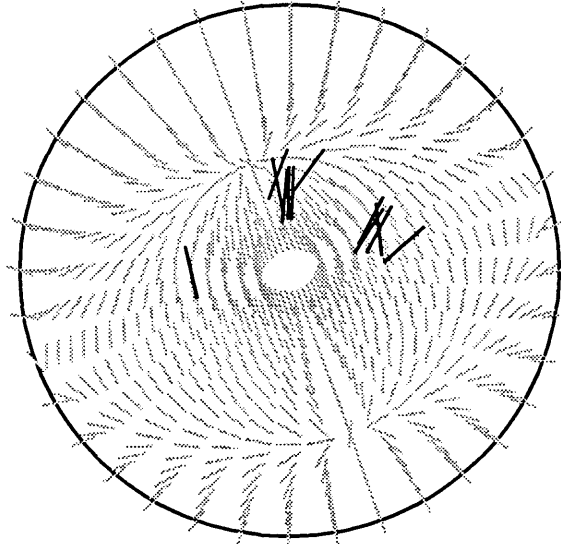


Figure 3.7: Lower hemisphere, equal area plot of observed and calculated double couple S-wave polarization directions for the March 11, 1957 (3:12:49 GMT) earthquake. Calculated directions are shown as gray lines. Observed are black lines.

tion directions do, however, provide constraints on the strike and dip of the solution, complementing P-wave first motion constraints on fault slip polarity.

Waveform Data

Lastly, we have access to microfilm records of seismograms stored at the World Data Center A (Glover, 1985). For the inversion, the selected waveforms must meet three basic criteria. First, P-waves in the distance ranges of less than 30° or greater than 90° are subject to the same problems as the S-waves at similar distances. Second, clock corrections and instrument response must be known. Third, the recording instruments must be

sensitive to ground motion with periods larger than 15 seconds. Table 3.1 lists stations meeting these criteria. Their azimuthal distribution relative to the earthquake of 3/11/57

Table 3.1: Stations used in this study

Station Code	Geographic Location	Latitude	Longitude
AAA	Alma Ata, Kazakhstan, CIS	43.272	76.950
HON	Honolulu, Hawaii, USA	21.322	-158.008
OTT	Ottawa, Ontario, Canada	45.394	-75.716
PAS	Pasadena, California, USA	34.148	-118.172
PUL	Pulkovo, Russia, CIS	59.773	30.324
SIM	Simferopol, Ukraine, CIS	44.950	34.117
TAS	Tashkent, Uzbekhstan, CIS	41.325	69.295
TIF	Tbilisi, Georgia, CIS	41.717	44.800
VLA	Vladivostok, Russia, CIS	43.120	131.893

(3:12:49 GMT) is shown in Figure 3.8. Note that even if this event is recorded by all of these stations, the azimuthal distribution of observations is poor. Because many of the events are not recorded at all of the stations, particularly the relatively noisy installation at HON, waveform inversion for source parameters, without application of a priori constraints, is nearly impossible. Fortunately, the first motion and S-wave polarization data provide excellent constraints on the strike, dip and slip of our solution. Using these a priori constraints, the relatively sparse waveform data can be inverted for the depth and seismic



Figure 3.8: Azimuthal equidistant plot, centered on the epicenter, of stations with available waveform data for the earthquake of 3/11/57 (3:12:49 GMT). The filled black circles represent the station locations. Circular arcs are spaced at 45° increments.

moment.

Determination and Use of A Priori Constraints

Figure 3.9 shows a lower hemisphere projection of the P-wave first motion and S-wave polarization data for an aftershock that occurred on March 3, 1957 (3:12:49 GMT). The solution shown in Figure 3.9 is typical for interplate thrust faulting earthquakes along the Aleutian arc. As mentioned previously, this solution does not match the P- or S-wave observations particularly well. No nodal plane separates the dilatational cluster to the east of the epicenter from the compressional field, and the calculated S-wave polarization

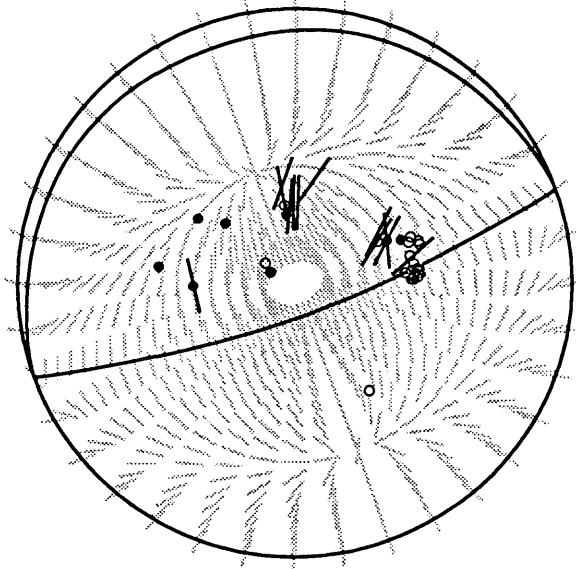


Figure 3.9: Lower hemisphere projection of observed P-wave first motion and S-wave polarization data for the earthquake of March 11, 1957 (3:12:49 GMT). The curved black lines represent P-wave nodal planes. All other symbols are as described in Figure 3.1 and Figure 3.6.

directions do not parallel those observed by Stauder and Udias (1963).

Simply changing the solution manually and inspecting the figure until an acceptable constraint is found is time consuming and difficult. To find the solution that minimizes the misfit between the observed and computed datasets, we formulate the problem by constructing a joint maximum likelihood function of the P-wave first motion and the S-wave polarization directions. Following Dillinger et al. (1971), we define, for the P-wave first motion directions, the maximum likelihood function over a discrete sample space as,

$$L(\bar{\beta}; \bar{X}_p) = Pr(\bar{X}_p | \bar{\beta}) = P^{R_p} (1 - P)^{N - R_p}, \quad \text{EQ 3.2}$$

where $\bar{\beta}$ is the vector containing the strike, dip, and slip of the solution, \bar{X}_p is the vector of observed first motion directions, P is the binomial probability of the pick being correct, and R_p is the number of agreements between the observed and predicted first motion directions. For the S-wave polarizations, we have, defined over a continuous sample space,

$$L(\bar{\beta}; \bar{X}_s) = \phi(\bar{X}_s | \bar{\beta}) = ce^{\left(-\frac{1}{2\sigma^2}R_s\right)}, \quad \text{EQ 3.3}$$

where \bar{X}_s is the vector of observed S-wave polarization angles, σ is the estimated standard deviation of the S-wave polarization angle, and R_s is the sum of the squares of the misfits between the observed and calculated polarization angles.

The joint maximum likelihood function, assuming independent errors in the two datasets, is

$$L(\bar{\beta}; \bar{X}_p, \bar{X}_s) = \phi r(\bar{X}_p, \bar{X}_s | \bar{\beta}) = P^{R_p} (1 - P)^{N - R_p} ce^{\left(-\frac{1}{2\sigma^2}R_s\right)}. \quad \text{EQ 3.4}$$

Note, ϕr plays the part of probability density for the S-wave data and probability function for the P-wave data.

Since the separate S-wave solution misfit, R_s , was a minimum in the maximum likelihood solution, we define $\bar{R}_p = N - R_p$ and substitute it into EQ 3.4 so that both \bar{R}_p and R_s decrease for better solutions. This leaves

$$L(\bar{\beta}; \bar{X}_p, \bar{X}_s) = cP^{N - \bar{R}_p} (1 - P)^{\bar{R}_p} e^{\left(-\frac{1}{2\sigma^2}R_s\right)}. \quad \text{EQ 3.5}$$

EQ 3.5 may be written as

$$L(\bar{\beta}; \bar{X}_p, \bar{X}_s) = ke^{(-R_{ps})}, \quad \text{EQ 3.6}$$

where

$$R_{ps} = a\bar{R}_p + bR_s \quad \text{EQ 3.7}$$

and

$$a = \ln\left(\frac{P}{1-P}\right), \quad b = \frac{1}{2\sigma^2}. \quad \text{EQ 3.8}$$

L is a maximum for R_{ps} a minimum, with a and b weighting each dataset.

The only ad hoc constraints for determining L are the probability of the P-wave first motion being correctly picked and the estimated standard deviation of the S-wave polarization data. Perhaps using a quantitative measure of the scatter in each data set as the weighting factor could help in constraining mechanisms with inconsistent P-wave first motions or S-wave polarizations directions, but, in selecting these values for each earthquake, a distinction has to be made between inconsistencies caused by mispicks and from those caused by source complications. For this reason, we choose to define standard errors for all of the solutions. The ad hoc values of $P=0.95$ and $\sigma=20^\circ$ are used since, for the events in this study, they determine solution spaces which best fit the observed S-wave polarizations directions without diminishing the importance of the P-wave first motions.

With these values, a 5° increment grid search is performed, using EQ 3.6, over all possible strike, dip, and slip combinations. For each solution, the location of the P and T axis, and the associated value of R_{ps} , are calculated. In order to establish a range of

acceptable P and T axis positions, a “percent-likelihood region” is created. Let

$$K = \sum_{\text{all } \bar{\beta}} L(\bar{\beta}; \bar{X}_p, \bar{X}_s) \quad \text{EQ 3.9}$$

where the summation is from the best $\bar{\beta}$ to the worst. We define the region R bounded by $L=\text{constant}$ such that

$$\sum_R \left(\frac{L}{K} \right) = 1 - \alpha \quad \text{EQ 3.10}$$

is a $100(1-\alpha)$ percent-likelihood region. For example, a 95% likelihood region contains solutions that make up 95% of the total likelihood of all solutions.

Figure 3.10 shows the lower hemisphere projection of the P and T axis positions for a corresponding percent likelihood region for the earthquake of 3/11/57 (3:12:49 GMT). The black region encloses 95% of the total likelihood. The gray and black region together include 99% and the white region makes up the remaining 1% of total likelihood. For this particular event, P-wave first motion and S-wave polarization directions provide tight constraints on source mechanism. This solution indicates tension down toward the north, which, if this event is in the lower plate, indicates downdip tension. In using this information for the waveform inversion, the a priori values for strike, dip, and slip are chosen from the average position of the P and T axes in the 95% likelihood region (Figure 3.11).

Waveform Inversion

The need for a priori constraints leads us to waveform invert those events only

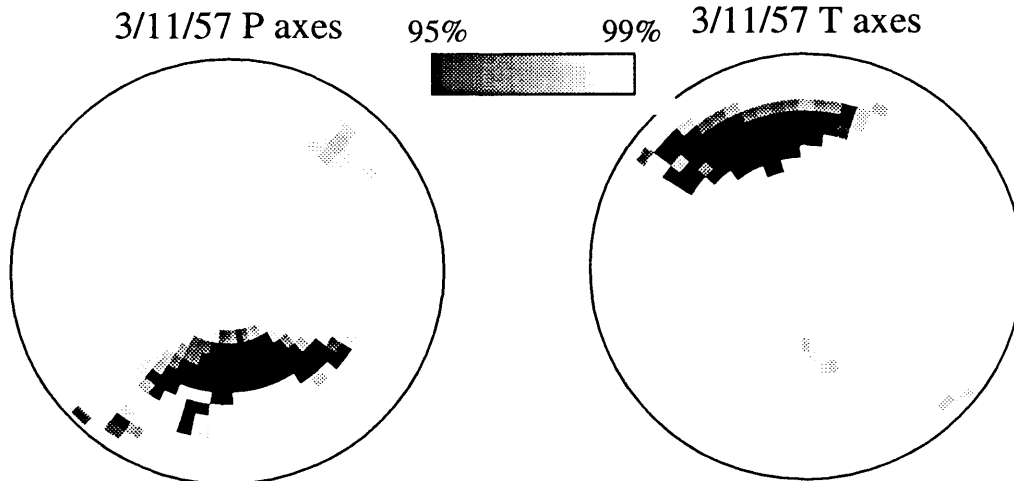


Figure 3.10: Percent-likelihood regions for the P (left) and T (right) axes positions for the earthquake of 3/11/57 (3:12:49 GMT). The entirely black region contains solutions which comprise 95% of the total likelihood. The grayscale includes extensions up to 99% of the total likelihood.

whose P and T axes have previously been tightly determined from the P-wave first motions and S-wave polarizations. For the present study, waveform inversion is used primarily to determine centroid depth and source-time function, and secondarily to determine fault strike, dip, and slip. Robust estimates of source depth and source-time function can usually be accomplished with at least two of the former USSR stations and the P-wave recorded at Pasadena. SH-wave information assists in making depth estimates because of the larger moveout of the depth phases from the S-wave. It is most important for confirming the strike, dip, and slip determined from the other two datasets.

With teleseismically recorded ($30^\circ \leq \Delta_P \leq 90^\circ$; $30^\circ \leq \Delta_{SH} \leq 80^\circ$) P-wave and SH-wave data, the inversion technique of Nabelek (1984) can simultaneously invert for

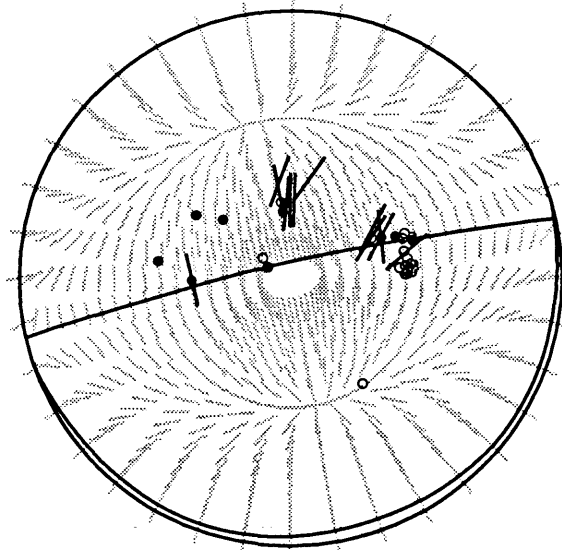


Figure 3.11: Average P and T axes solution for the earthquake of 3/11/57 (3:12:49 GMT). All symbols are as described in Figure 3.7.

centroid depth, the far field source-time function, seismic moment, and the strike, dip, and slip of an earthquake. The inversion iteratively minimizes the sum of the squares of the error between the data and the synthetics, normalizing the output waveforms to a common instrument magnification (3000) and epicentral distance ($\Delta=60^\circ$).

Instrument parameters for the stations used in this study are shown in Table 3.2 and are obtained from the microfilm records. T and l represent the period (s) and damping (g) of the seismometer and galvanometer, respectively. The number in parentheses after the gain is the period (in seconds) at which it was measured. For Honolulu, the number in the l_s column represents the damping ratio.

The crustal structure assumed at the source and receiver is a half space, with

Table 3.2: Instrument Parameters

Station Code	Instrument Type	Direction	T_s	T_g	l_s	l_g	Gain (period)
AAA	Kirnos	N-S	12.5	1.0	0.46	5.0	1509(1.4)
		E-W	12.5	1.0	0.46	5.0	1509(1.4)
		Z	12.5	1.0	0.46	5.0	1001(7)
HON	Milne-Shaw	N-S	12.0	N/A	20.0	N/A	155
	Milne-Shaw	E-W	12.0	N/A	20.0	N/A	155
OTT	Benioff	Z	1.0	75.0	0.7	1.0	2550(1)
PAS	Benioff	Z	1.0	90.0	1.0	1.0	3000(1)
PUL	Galitzin	Z	9.5	9.4	1.0	1.0	724(7)
SIM	Kirnos	Z	12.6	1.2	0.45	5.1	1506(7)
TAS	Kirnos	Z	12.4	12.6	1.0	1.0	753(7)
TIF	Galitzin	Z	12.6	12.4	1.0	1.0	1125(7)
VLA	Kirnos	Z	12.5	1.2	0.45	4.9	1092(7)

$\alpha=6.60$ km/sec, $\rho=2.9$ gm/cm³, and $\sigma=0.25$. The relocated epicenter of each event (Boyd et al., 1993) and a bathymetric map of the Aleutian Arc (Swenson, 1982) are used to determine the depth of the water layer above the source. All depths reported here are computed from the top of the water layer. Since the velocity structure is very simple, care must be taken not to interpret complexities in the waveform, most likely caused by unmodeled velocity structure, as moment release. Also, when the duration of the source time function exceeds the differential travel time between the body wave and its depth phase, estimates of the centroid depth become difficult. To avoid these problems, all waveform inversion is

performed assuming simple, i.e. short, source-time functions. As an example, the waveform solutions for 3/11/57 (3:12:49 GMT) are shown in Figure 3.12. This solution corre-

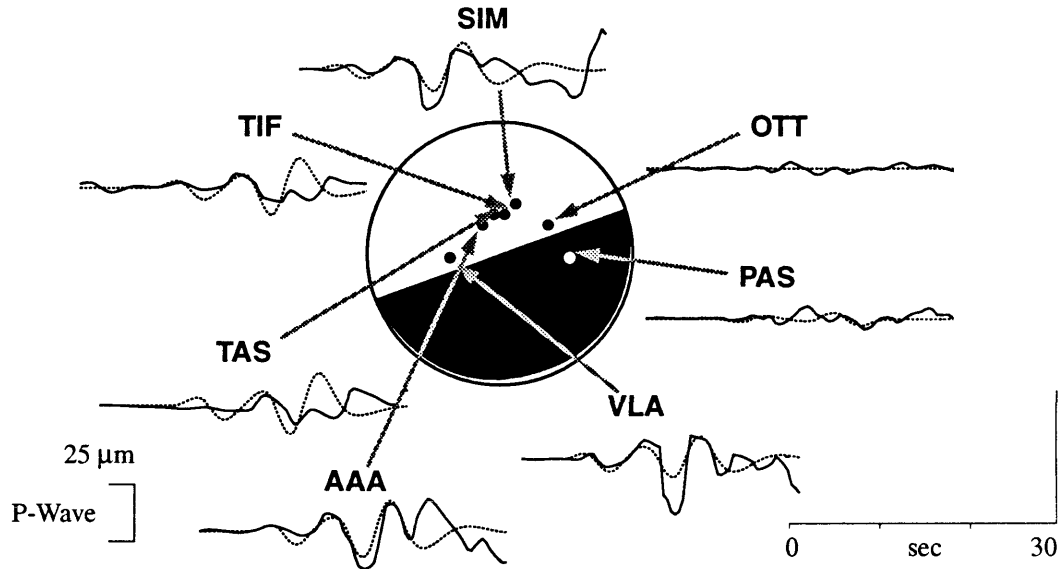


Figure 3.12: Waveform solution for the earthquake of 3/11/57 (3:12:49 GMT). Station name abbreviations are given in Table 3.1. Amplitude (normalized to an instrument 60° from the source with a gain of 3000) and time scale is shown in the lower right hand corner.

sponds to a strike, dip, and slip of 72° , 5° , and -95° , and a depth and magnitude of 30 km and 3.0×10^{26} dyne-cm². Further discussion of the tectonic implications and comparison of this result with that of Stauder and Udias will be discussed in Chapter 4.

Solution Error Bounds

For events with S-waveforms, error bounds for all parameters, except centroid

depth, are calculated assuming that errors in the waveform data are Gaussian distributed, and the bounds represent the one σ region of that curve. Centroid depth error bounds are calculated by assuming a 10% error in the velocity model.

For events without S-waveforms, error bounds for depth and seismic moment are determined as before. Only a qualitative bound is placed on the strike, dip, and slip, relative to the scatter in the P- and T-axes plots, i.e. less scatter implies a more reliable solution.

CHAPTER 4

DISCUSSION

Using the selection criteria outlined in Chapter 3, eight aftershocks (outlined in Table 4.1) of the 1957 event are modeled. (Details of the solutions, plots of the P and T

Table 4.1: Event Locations and Origin Times

Number	Date	Origin Time	Latitude	Longitude
1	March 9,1957	20:39:23.92	52.335	-169.568
2	March 11,1957	03:12:48.86	50.889	-177.182
3	March 11,1957	14:55:26.42	51.156	-178.519
4	March 14,1957	14:47:52.09	51.122	-176.708
5	March 15,1957	02:52:16.35	52.652	-166.937
6	March 22,1957	14:21:13.93	53.624	-165.686
7	April 19,1957	22:19:35.48	52.160	-166.305
8	June 13,1957	10:40:46.03	51.366	-175.129

axes constraints, agreement with observed P-wave first motion and S-wave polarization directions, and waveform fits are shown in the Appendix). Some of these solutions are a result of direct application of the method outlined in Chapter 3, although most required additional information to accurately constrain all source parameters, and none are deter-

mined in exactly the same manner. To illustrate these differences, we compare and contrast the solutions of Stauder and Udias to those determined in this study.

Method Effectiveness and Comparison with the Results of Stauder and Udias

Stauder and Udias (1963) decided that accurate source mechanism determination would need to include P- and S-wave information (as explained in Chapter 3), rather than use P-wave first motions alone (e.g. Hodgson, 1957). In their study of circum-pacific earthquakes, Stauder and Udias separated the events into three groups and a variant of the first, based on similarities in the S-wave polarization directions. Group I has S-wave polarization directions observed in Europe and North America that are oriented to the northeast in Europe and to the northwest for the US stations. Group II earthquakes have S-wave polarization directions oriented sub-parallel to each other. The variant of the first group has P-wave data that constrain only one nodal plane but the S-wave polarization directions match those of the first group. No events modeled in this study are from Group III, and hence will not be considered here. Group I and its variant contain double couple solutions, while groups II and III include single couple solutions like those assumed by Hodgson (1957). As shown in Figure 4.1, the mechanisms are predominantly strike-slip, probably in an effort to match the mechanisms of Hodgson (1957).

Our method uses the datasets of Stauder and Udias (1963) to create a priori constraints on the P and T axes, allowing for much quicker modeling of the observed waveforms. As explained in Chapter 3, initial attempts to waveform model these events with a priori constraints determined graphically were unsuccessful, since it appeared many solu-

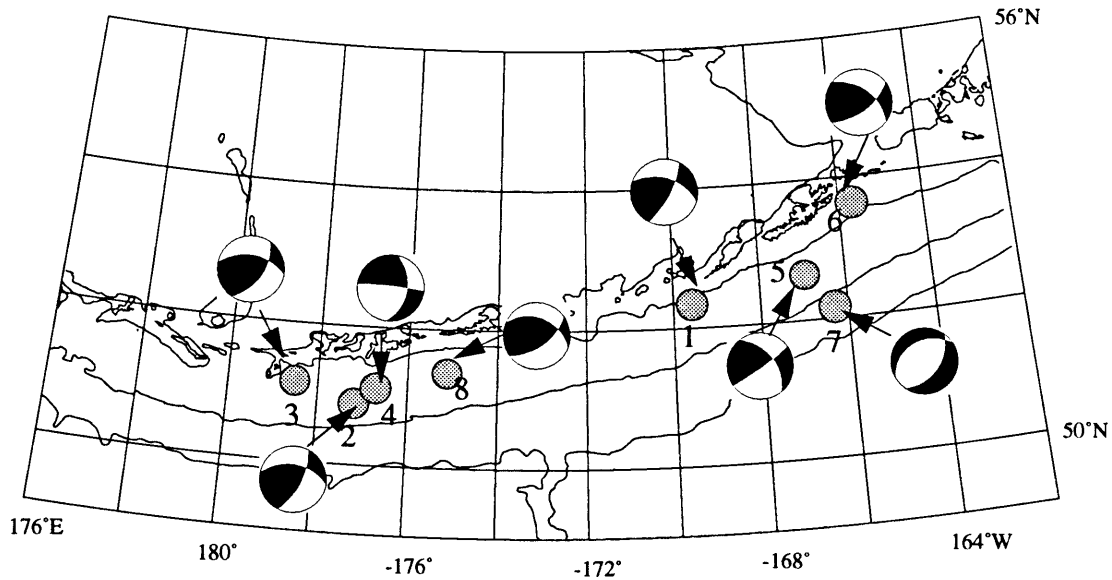


Figure 4.1: Source mechanisms as determined by Stauder and Udias (1963). 400 m bathymetry contours border the arc and 6000 m contours border the trench. Epicenter locations are from Boyd et al.(1993). Source mechanisms are lower hemisphere projections, with shaded compressional quadrants. Event numbers correspond to Table 4.1.

tions satisfied the P-wave first motions and S-wave polarization directions, but few of those matched the waveforms. As an example, Figure 4.2 compares our solution with that determined by Stauder and Udias for event 3. Inspection shows our solution is apparently only a slight improvement over the mechanism proposed by Stauder and Udias. Also, graphical agreement of calculated and observed P-wave first motions does not appear significantly different for either solution.

Fortunately, the relative value of R_{ps} , the “score” used in the maximum likelihood calculation (Chapter 3), quantifies the error in each solution, giving clear indication that

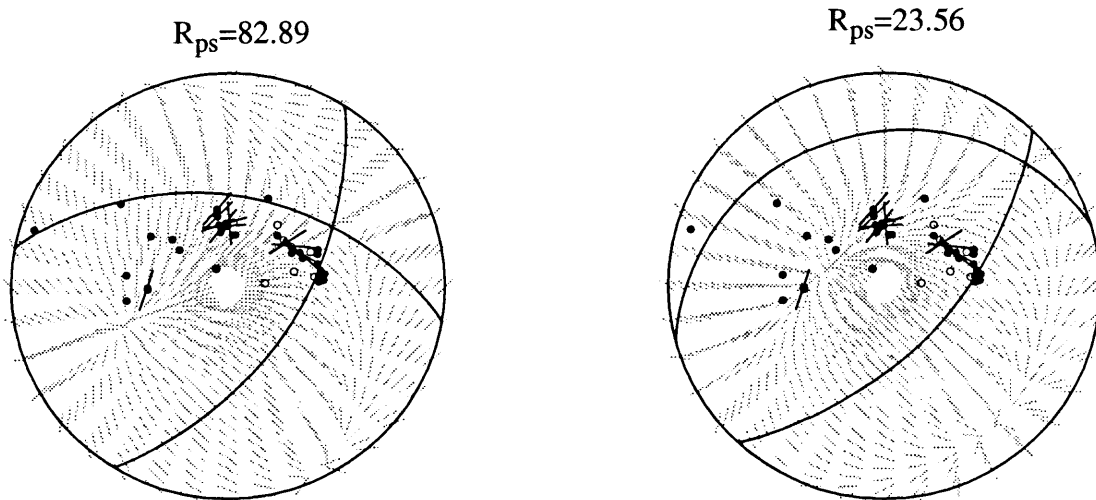


Figure 4.2: Results of Stauder and Udias (left) and this study (right) for the Group I earthquake of 3/11/57 (14:55:26.42 GMT). Included is the relative value of R_{ps} for each solution. All symbols are as described in Figure 3.9.

our mechanism better fits the observed P-wave first motions and S-wave polarization directions. The difference in score is primarily due to the better agreement in S-wave polarization directions observed in North America, and secondarily to the slight improvement in polarization directions observed in Europe. Stauder and Udias' solution appears to be biased by the single S-wave polarization direction observed to the west of the epicenter in Hong Kong. The R_{ps} values (Figure A.8) suggest a small strike slip component for this earthquake, unlike the large strike slip component inferred by Stauder and Udias. (Note, the R_{ps} values are not normalized, and comparisons can only be made between R_{ps} values for solutions with the same P-wave first motions and S-wave polarization directions.)

Although our method quickly constrains the fault plane orientation for these after-

shocks, the quality of these constraints varies relative to the patterns in S-wave polarization directions observed by Stauder and Udias (1963). For example, the group II earthquakes of 3/11/57 (3:12:48.86 GMT) and 3/14/57 have the best P and T axes constraints of the earthquakes in this study (Figure A.5 and Figure A.11). The S-wave polarization directions for events 2 and 4 all roughly trend north-south, constraining one nodal plane to lie perpendicular to them. Likewise, the cluster of P-wave first motions to the east of each epicenter are consistent with the nodal plane location predicted by the S-waves. This nearly vertical plane results in *P* and *T* axes oriented away from the normal, and small changes in the strike of these solutions creates large changes in the misfit.

Unlike Group II, Group I events, with nearly vertical pressure or tension axes (e.g. events 7 and 8), have P-wave first motions and S-wave polarization directions that are relatively symmetric about the point where the axis exits the lower hemisphere (e.g. Figure A.22). This allows the strike of the solution to rotate greatly while still matching the observed data. Thus, constraining only the non-vertical axis to the horizontal plane (Figure A.20 and Figure A.23). The a priori strike for the remaining Group I events (3 and 6) are better constrained, but still allow a large range of possible fault plane orientations. Fortunately, the strike for these events are constrained by SH-waveforms. Without this waveform data, no well determined source mechanism can be proposed.

Stauder and Udias' variant of Group I (Figure 4.2) contains the most problematic mechanisms determined in this study. As discussed later in this chapter, the mechanism proposed for the event of 3/9/57 is difficult to interpret. Similar to the study of Stauder and Udias (1963), considerable effort was expended in trying to model event 1 to match previ-

ous solutions (like those of Ekström and Engdahl, 1989), but to no avail. The large differential in relative R_{ps} value for the mechanism of Stauder and Udias (Figure 4.2) gives us greater confidence our solution. In addition, the P and T axes constraints (Figure A.2) indicate tension down toward the north and place the pressure axis in the horizontal plane

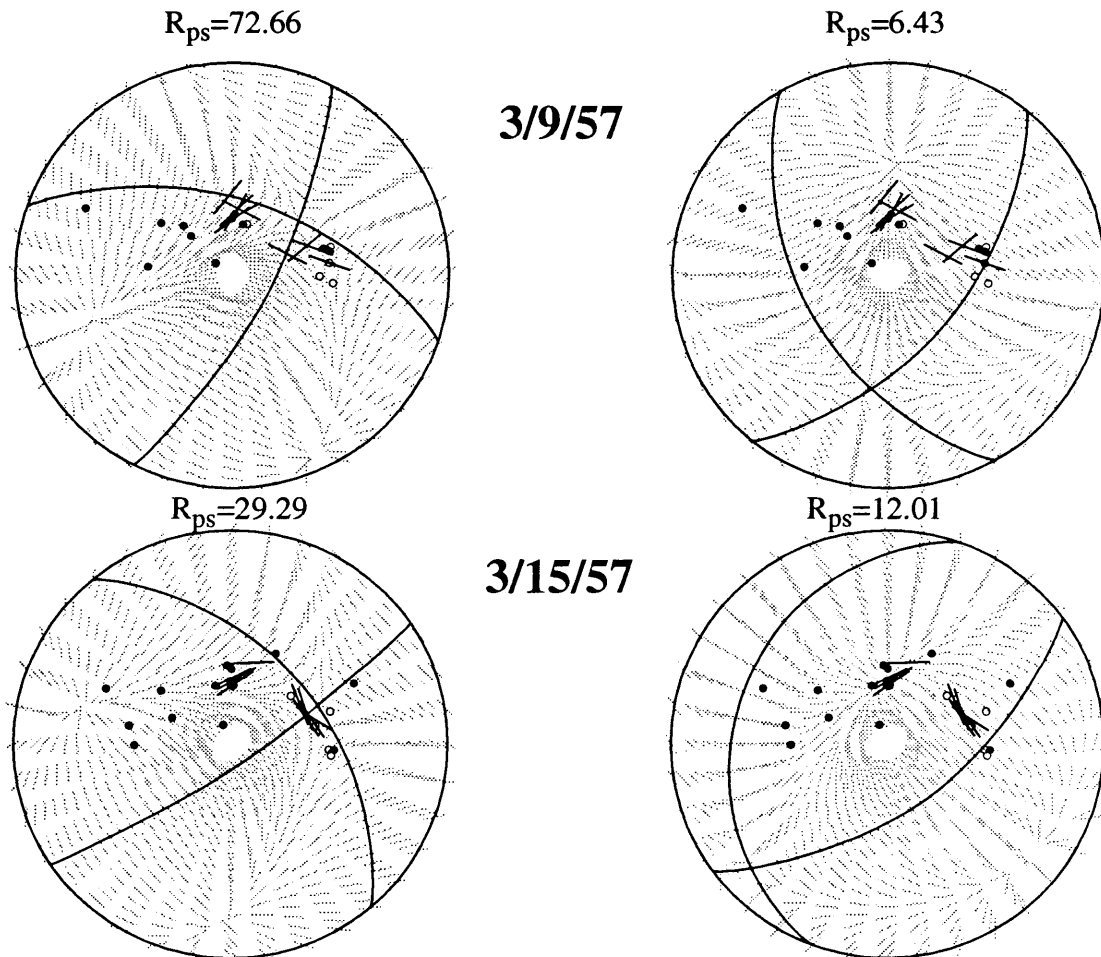


Figure 4.3: Results of Stauder and Udias (left) and this study (right) for the earthquakes of their Group I variant. All symbols are as described in Figure 3.9.

roughly trending east-west, like the mechanism we propose. This fault plane solution also matches the SH waveforms (Figure A.3), and the P-waves indicate a source depth of 32 km. From this, regardless of the tectonic implications, the mechanism for event 1 is well

constrained. The observed data, however, could be unreliable because of this event's temporal proximity to the mainshock (approximately 6 hours later), but determining this requires access to the original records for all of the datasets from this event, which is not possible.

Also critical in selecting our solution for event 5 are the station clock corrections (up to 35 seconds) that are listed on the seismogram. The waveforms for this earthquake (Figure A.15) are emergent, suggesting either source complexity or a strike-slip fault plane. To distinguish between these two cases, the actual arrival time for the phases are very important, as visually determining the first break is difficult. If the traveltimes corrections are not applied to the digitized waveforms, errors in start times complicate aligning the synthetic seismograms to corresponding phases in the observed waveform, i.e. the arrival you are modeling as P at one station may correspond to pP at another. This causes an anticorrelation in the synthetics, making inversion of these waveforms impossible.

Tectonic Interpretations

Source mechanisms for the eight events studied here are shown in Figure 4.4, with the event numbers corresponding to those of Table 4.1. Of the modeled events, all but three (1, 2, and 4) are consistent with expected mechanisms and are located in the Outer Arc Rise and the MTZ.

Trench and Outer Arc Rise

Only one event from this study (7) occurred along the outer arc rise. Its source

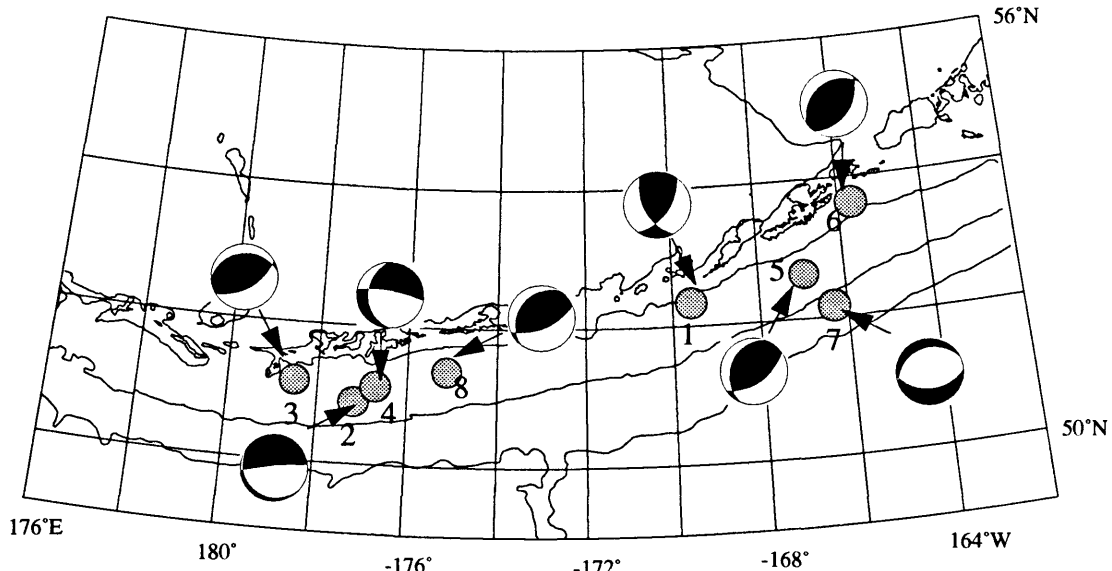


Figure 4.4: Source mechanisms determined in this study. All symbols are as described in Figure 4.1.

mechanism and depth, 12 km (Figure 4.6), are similar to those determined by other investigators for outer arc events (Ekström and Engdahl, 1989; House and Jacob, 1983; Stauder 1968, 1972). In general, these focal mechanisms have tension axes oriented within 10° to 30° of the normal to the trench axis and nearly vertical pressure axes. These events have been interpreted as indicating high tensile stresses caused by the bending of the subducting Pacific plate (Stauder, 1968; Ekström and Engdahl, 1989). The close temporal association between outer arc rise activity and great thrust zone earthquakes (e.g. Spence, 1987), however, suggests that these extensional events may be related to movement on the main thrust zone, as compressional stresses are relieved by the mainshock, putting the outer arc portion of the Pacific plate into tension.

Main Thrust Zone

Like the main thrust zone mechanisms determined in earlier studies (Ekström and Engdahl, 1989; House and Jacob, 1983; Stauder 1968, 1972) events 3, 5, 6, and 8 (Figure 4.4) have slip directions oriented slightly northwest of the normal to the trend of the trench. Cross sections of seismicity from the Adak Island local network (Figure 4.5, Ekström and Engdahl, 1989) and the Unalaska local network (Figure 4.6, Boyd and Jacob,

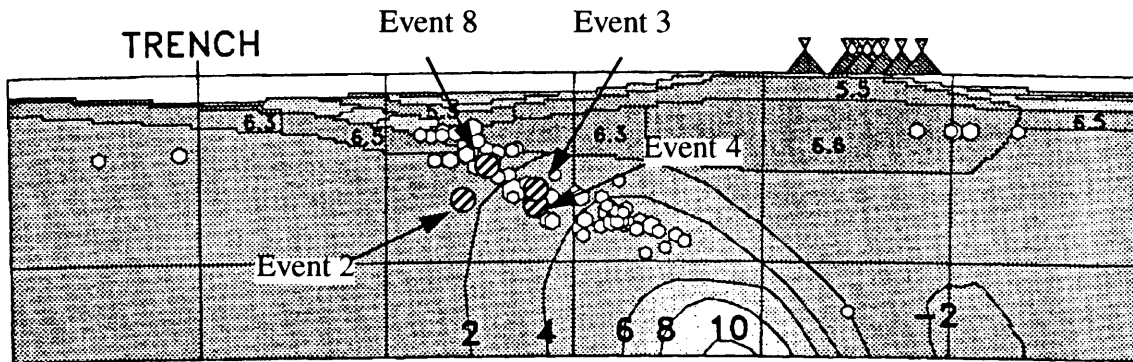


Figure 4.5: Cross sectional view of seismicity of the Adak Island region from the study of Ekström and Engdahl (1989). Events 2, 3, 4, and 8 are the striped circles labeled in the figure. The grid spacing is 50 km. The relocated hypocenters and locations of the volcanoes are rotated into a plane locally perpendicular to the arc (Figure modified from Ekström and Engdahl, 1989).

1986) indicate the depths and locations of these events are consistent with activity located along the MTZ.

Of the four events mentioned above, only event 6 occurred outside of the coseismic rupture area of the 1957 event (e.g. Lane, 1992; Satake and Johnson, 1992), on the eastern side of the Unalaska Gap. Seismicity in the Unalaska region did not initiate until

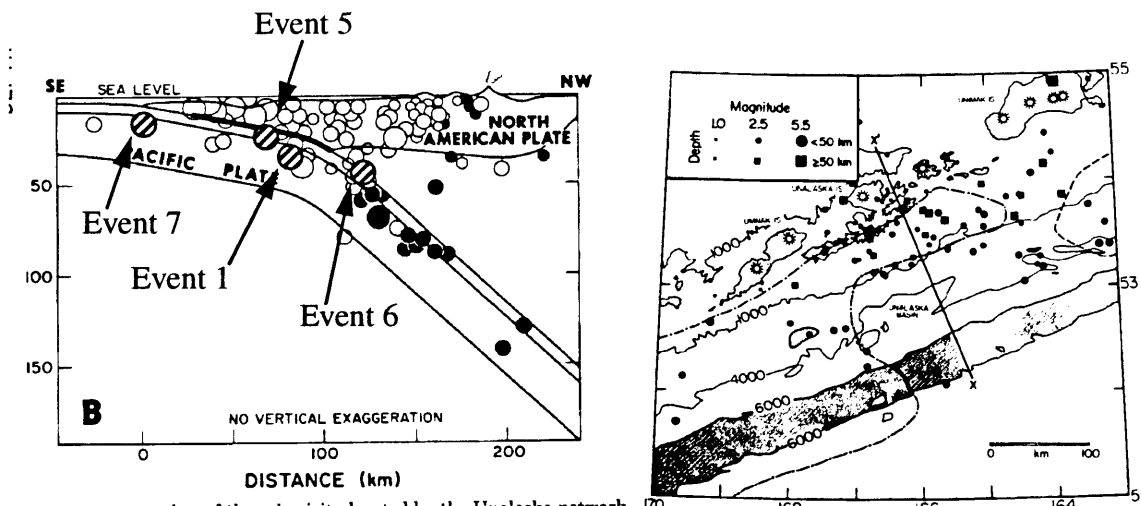


Figure 4.6: (left) Depth of events 1, 5, 6, and 7 relative to the depths recorded by the Unalaska seismic network. The mechanism is a back hemisphere projection in the plane of the cross section indicated by XX' in the map on the right (modified from Boyd and Jacob, 1986).

54 hours after the 1957 mainshock, and was concentrated within a small region just east of Unalaska Island (House et al., 1981; Boyd et al., 1993). From this information, we cannot unambiguously determine if the Unalaska region ruptured as a result of the 1957 earthquake. If it did so, rupture would have to propagate through the Unalaska region with either a slow rupture velocity or long rise time, both alternatives suggesting the Unalaska region is weakly coupled across the MTZ. If rupture did not propagate through the Unalaska region, earthquakes like event 6 might indicate the development of a stress concentration around Unalaska Island, suggesting the possible occurrence of a large earthquake in this region in the near future.

Anomalous Events

The remaining events (1, 2, and 4) are quite different from the others located along the MTZ, and bear further discussion. Event 1 occurs about 32 km beneath the ocean surface, which, according to the seismicity cross section of Boyd and Jacob (1986) (Figure 4.6), places it in the lower plate. Near event 1, House and Jacob (1983) describe an earthquake with a source mechanism of similar fault plane orientation, but with opposite slip polarity, that they tentatively place in the upper plate (30 km). What relationship this earthquake has with our lower plate event is unclear. Ekström and Engdahl (1989) and Engdahl et al. (1989) mention two mechanisms similar to event 1 occurring in the quiescent time period before the mainshock of 1986. All of these events have pressure or tension axes that are oriented 90° from that expected for main thrust zone events and occur at depths near the MTZ making assignment to the upper or lower plate difficult. With the few source mechanisms we have for this region, it is difficult to define unique tectonic mechanisms for earthquakes like event 1.

Based on their hypocentral locations (Figure 4.5) and source mechanisms (Figure 4.4), events 2 and 4 represent downdip tension in the subducting Pacific plate. One possible interpretation of these events is the existence of a strongly coupled portion of the MTZ, updip of their locations, that did not rupture during the 1957 event. In this model, these earthquakes result from slab pull forces associated with the downgoing plate, much like those used to explain normal faulting events in the outer arc high after great earthquakes (Spence, 1987). Ryan and Scholl (1993) suggest the portion of the arc beneath Hawley Ridge, which ruptured during the 1986 event, is strongly coupled to the downgo-

ing plate. This geologic asperity is based on evidence indicating the fault surface in this region is smoother and more coupled than the surrounding interface. If this is the case, the 1986 event may be in essence an aftershock of the 1957 great earthquake, relieving stresses applied as the 1957 event ruptured the weaker portions of the fault interface around Hawley Ridge.

CHAPTER 5

CONCLUSIONS

Combining P-wave first motions and S-wave polarization directions, maximum likelihood regions are constructed that constrain the locations of P and T axes, and thus the orientation of the fault plane's strike, dip, and slip direction. These are used as a priori information for waveform inversion of source parameters. In this scheme, the waveforms provide strongest constraints on the depth, magnitude, and source time function, and, for events with SH waveforms, independent confirmation of the a priori fault geometry.

Unlike graphical methods, quantifying the misfit between observed and calculated P-wave first motion and S-wave polarization directions provides quick determination of the best a priori constraints. The quality of these constraints, however, is dependent on the orientation of the *P* and *T* axes for the aftershock. For a priori pressure and tension axes located away from vertical, the fault plane is tightly constrained. If, however, one of the axes is nearly vertical, symmetry in the datasets provides little control of the a priori strike. For the earthquakes with these poor a priori constraints or complicated waveforms, additional information, such as SH waveforms and station clock corrections, are required for well constrained fault plane estimates.

Using this method, source mechanisms are determined for eight aftershocks of the March 9, 1957 great earthquake. Four of the mechanisms are consistent with MTZ thrust faulting and one Outer Arc Rise normal faulting event is modeled. A thrust faulting event

determined along the Unalaska Gap does not uniquely determine the behavior of this region. The two events occurring near Adak Canyon, however, indicate down dip tension in the downgoing plate. This could be due to the high shear strength of the fault beneath Hawley Ridge, suggesting the 1986 event was an aftershock of the 1957 great earthquake.

REFERENCES CITED

- Abe, K. 1972. Lithospheric normal faulting beneath the Aleutian trench. *Phys. Earth and Planetary Int.* 5: 190-198.
- Aki, Keiiti and Paul G. Richards. 1980. *Quantitative Seismology: Theory and Methods*. Volume 1. New York, NY. W. H. Freeman and Company.
- Benioff, Hugo. 1954. Orogenesis and deep crustal structure-Additional evidence from seismology. *Bull. Geol. Soc. Am.* 65: 385-400.
- Boyd, Thomas M. 1985. Characteristics of seismicity associated with the 1957 ($M_w=9.1$) Aleutian Islands earthquake (abstract). *EOS*. 66: 298.
- Boyd, Thomas M. and F. Abers. 1992. Seismotectonics, seismic history, and earthquake potential of the eastern Aleutian seismic gaps: Shumagin and Unalaska. *Wadati Conference on Great Subduction Earthquakes*. Abstract. Fairbanks, Alaska. Geophysical Institute, University of Alaska. 136-139.
- Boyd, Thomas M., and Kenneth C. Creager. 1991. The Geometry of Aleutian Subduction: Three-Dimensional Seismic Imaging. *J. Geophys. Res.* 96: 2267-2291.
- Boyd, Thomas M., E. R. Engdahl, and W. Spence. 1992. Analysis of seismicity associated with a complete seismic cycle along the Aleutian arc: 1957 through 1989. *Wadati Conference on Great Subduction Earthquakes*. Abstract. Fairbanks, Alaska. Geophysical Institute, University of Alaska.
- Boyd, Thomas M., E. R. Engdahl, and W. Spence. 1993. A Complete Seismic Cycle along

- the Aleutian Arc?: Analysis of seismicity from 1957 through 1989. In preparation.
- Boyd, Thomas M. and Klaus Jacob. 1986. Seismicity of the Unalaska Region, Alaska. *Bull. Seism. Soc. Am.* 76: 463-481.
- Boyd, Thomas M. and John L. Nabelek. 1988. Rupture Process of the Andreanof Island Earthquake of May 7, 1986. *Bull. Seism. Soc. Am.* 78: 1653-1673.
- Bulletin Mensuel de Bureau Central International de Seismologie. January-June 1957. Union Geodesique et Geophysique Internationale, Strasbourg, France.
- Byerly, P. 1955. Nature of faulting as deduced from seismograms, in Poldervart, Arie (editor), *Crust of the earth*. Geol. Soc. Am. Special Paper 62. 75-85.
- Creager, Kenneth C., and Thomas M. Boyd. 1991. The Geometry of Aleutian Subduction: Three-Dimensional Kinematic Flow Model. *J. Geophys. Res.* 96: 2293-2307.
- Das, S., and B. V. Kostrov. 1990. Inversion for seismic slip history and distribution with stabilizing constraints: Application to the 1986 Andreanov Islands earthquake. *J. Geophys. Res.* 95: 6899-6913.
- Dillinger, William H., Allen J. Pope, and Samuel T. Harding. 1971. *The Determination of Focal Mechanisms using P- and S-Wave Data*. Rockville, MD: United States Department of Commerce.
- Ekström, G., and E.R. Engdahl. 1989. Earthquake source parameters and stress distribution in the Adak Island region of the central Aleutian Islands, Alaska. *J. Geophys. Res.* 94: 15,499-15,519.
- Engdahl, E. R., and D. Gubbins. 1987. Simultaneous travel time inversion for earthquake location and subduction zone structure in the central Aleutian Islands. *J. Geophys.*

- Res.* 92: 13,855-13,862.
- Engdahl, E. R., S. Billington, and C. Kisslinger. 1989. Teseleismically reecorded seismicity before and after the May 7, 1986, Andreanof Islands, Alaska, earthquake. *J. Geophys. Res.* 94: 15,481-15,498.
- Fowler, C. M. R. 1990. *THE SOLID EARTH: An Introduction to Global Geophysics*. Cambridge, England. Cambridge University Press.
- Frohlich, C., S. Billington, E. R. Engdahl, A. Malaoff. 1982. Detection and location of earthquakes in the central Aleutian subduction zone using land and ocean bottom seismograph stations. *J. Geophys. Res.* 87: 6853-6864.
- Gates, G. and W. Gibson. 1956. Interpretation of the configuration of the Aleutian Ridge. *Geol. Soc. Am. Bull.* 67: 127-146.
- Geist, Eric, L., Jonathan R. Childs, and David W. Scholl. 1988. The origin of summit basins of the Aluetian ridge: Implications for block rotation of an arc massif. *Tectonics*. 7: 327-341.
- Glover, D. P., H. Meyers, R. B. Haberman, and M. Whittington. 1985. Inventory of filmed historical seismograms and station bulletins at World Data Center A. *World Data Center A Report SE-37*.
- Grim, P. J. and B. H. Erickson. 1969. Fracture zones and magnetic anomalies south of the Aleutian Trench. *J. Geophys. Res.* 74: 1488-1494.
- Gubbins, David. 1990. *Seismology and Plate Tectonics*. Cambridge, England. Cambridge University Press.
- Gutenberg, B. 1955. The first motion in longitudinal and transverse waves of the main

- shock and the direction of slip, in Oakeshott, Gordon B. (editor) Earthquakes in Kern County, California during 1952. *Calif. Division of Mines Bulletin*. 171: 165-170.
- Hodgson, John H. 1957. Nature of faulting in large earthquakes. *Geol. Soc. America Bull.* 68: 611-644.
- Horowitz, F. G., and A. Ruina. 1989. Slip patterns in a spatially homogeneous fault model. *J. Geophys. Res.* 94: 10,279-10,298.
- House, L. S. and K. H. Jacob. 1983. Earthquakes, plate subduction, and stress reversals in the eastern Aleutian arc. *J. Geophys. Res.* 88: 9347-9373.
- House, L. S., L. R. Sykes, J. N. Davies, and K. H. Jacob. 1981. Identification of a possible seismic gap near Unalaska Island, eastern Aleutians, Alaska. In *Earthquake Prediction-An International Review. Maurice Ewing Series 4*. American Geophysical Union, Washington D. C.
- Houston, H. and E. R. Engdahl. 1989. A comparison of the spatio-temporal distribution of moment release for the 1986 Andreanof Islands earthquake with relocated seismicity. *Geophys. Res. Lett.* 16: 1421-1424.
- International Seismological Summary. 1957. Kew Observatory, Surrey, England.
- Jacob, K. H. 1984. Estimates of long term probabilities for future great earthquakes in the Aleutians. *Geophys. Res. Lett.* 11: 295-298.
- King, G. C. P. 1986. Speculations on the geometry of the initiation and termination processes of earthquake rupture and its relation to morphology and geological structure. *Pageoph.* 124: 567-585.

- King, G. C. P., and J. Nabelek. 1985. The role of bends in faults in the initiation and termination of earthquake rupture. *Science*. 228: 984-987.
- Lane, F. D. 1992. Estimation of kinematic rupture parameters from historical seismograms: An application of simulated annealing to a nonlinear optimization problem. CSM Thesis T-4133.
- Lay, T., L. Ruff, and H. Kanamori. 1980. The asperity model and the nature of large earthquakes in subduction zones. *Earthquake Pred. Res.* 1: 3-71.
- Lonsdale, P. 1988. Paleogene history of the Kula plate: Offshore evidence and onshore implications. *Geol. Soc. Am. Bull.* 100: 733-754.
- Mogi, K. 1969. Relationship between the occurrence of great earthquakes and tectonic structures. *Bull. Earthq. Res. Inst. Tokyo Univ.* 47: 429-451.
- Nabelek, John L. 1984. *Determination of Earthquake Source Parameters From Inversion of Body Waves*. Ph.D. Dissertation. Massachusetts Institute of Technology.
- Nakano, H. 1923. Notes on the nature of the forces which give rise to the earthquake motions. Central Meteorol. Observatory of Japan Seismol. Bull. 1. 92-120.
- Newberry, James T., David L. LaClair, and Kazuya Fujita. 1986. Seismicity and tectonics of the far western Aleutian Islands. In: G. L. Jounhson and K. Kaminuma (editors), *Polar Geophysics. Jour. of Geodynamics.* 6: 13-32.
- Nishenko, S. P., and K. H. Jakob. 1990. Potential during the next 20 years for large and great earthquakes in the Queen Charlotte-Alaska-Aleutian seismic zone. *J. Geophys. Res.* 95: 2511-2532.
- Reyners, M. and K. Coles. 1982. Fine structure of the dipping seismic zone and subduc-

- tion mechanics in the Shumagin Islands, Alaska. *J. Geophys. Res.* 87: 356-366.
- Richter, Charles F. 1958. *Elementary Seismology*. San Francisco, California. W. H. Freeman and Company.
- Romney, C. 1956. Seismic evidence for the direction of faulting in the Fairview Peak earthquake (Abstract). *Geol. Soc. America Bull.* 67: 1782.
- Ruff, L., and H. Kanamori. 1983. The rupture process and asperity distribution of three great earthquakes from long period diffracted P-waves. *Phys. Earth and Planet. Inter.* 31: 202-230
- Ryan, H. F. and D. W. Scholl. 1993. Geologic implications of great interplate earthquakes along the Aleutian Arc. In preparation.
- Ryan, H. F. and D. W. Scholl. 1989. The evolution of fore-arc structures along an oblique convergent margin, central Aleutian arc. *Tectonics.* 8: 497-516.
- Satake, Kenji, and Jean M. Johnson. 1992. Source parameters of the 1957 Aleutian earthquake from tsunami records. *Wadati Conference on Great Subduction Earthquakes*. Abstract. Fairbanks, Alaska. Geophysical Institute, University of Alaska. 5-6.
- Spence, William. 1987. Slab Pull and the Seismotectonics of Subducting Lithosphere. *Reviews of Geophysics.* 25: 55-69.
- Stauder, William. 1968. Tensional Character of Earthquake Foci beneath the Aleutian Trench with Relation to Sea-Floor Spreading. *J. Geophys. Res.* 73: 7693-7701.
- Stauder, William. 1972. Fault Motion and Spatially Bounded Character of Earthquakes in Amchika Pass and the Delarof Islands. *J. Geophys. Res.* 77: 2072-2080.

- Stauder, William, and G. A. Bollinger. 1964. *The S Wave Project for Focal Mechanism Studies: Earthquakes of 1962*. St. Louis University.
- Stauder, William, and G. A. Bollinger. 1966. The S Wave Project for Focal Mechanism Studies: Earthquakes of 1963. *Bull. Seism. Soc. Am.* 56: 1363-1371.
- Stauder, William, and Agustin Udias. 1963. S-Wave Studies of Earthquakes of the North Pacific, Part II: Aleutian Islands. *Bull. Seism. Soc. Am.* 53: 59-77.
- Swenson, Phyllis, and Tau Rho Alpha. 1982. Equal area base map of Alaska and Northeast Siberia. USGS open file 78-82 map. US Dept. of the Interior. Washington, D.C.
- Sykes, L. R. 1971. Aftershock zones of great earthquakes, seismicity gaps, and earthquake prediction for Alaska and the Aleutians. *J. Geophys. Res.* 76: 8021-8041.
- Taber, J. J., S. Billington, and E. R. Engdahl. 1991. Seismicity of the Aleutian Arc, in Slemmons, D. B., E. R. Engdahl, M. D. Zoback, and D. D. Blackwell, eds. *Neotectonics of North America. Decade Map Volume 1*. Boulder, Colorado. Geological Society of America.
- Thatcher, W. 1990. Order and diversity in the modes of circum-Pacific earthquake recurrence. *J. Geophys. Res.* 95: 2609-2623.

APPENDIX

This appendix contains source information for the events shown in Figure A.1 and Table A.1. Methodology used in determining the source mechanisms and errors is that described in Chapter 3.

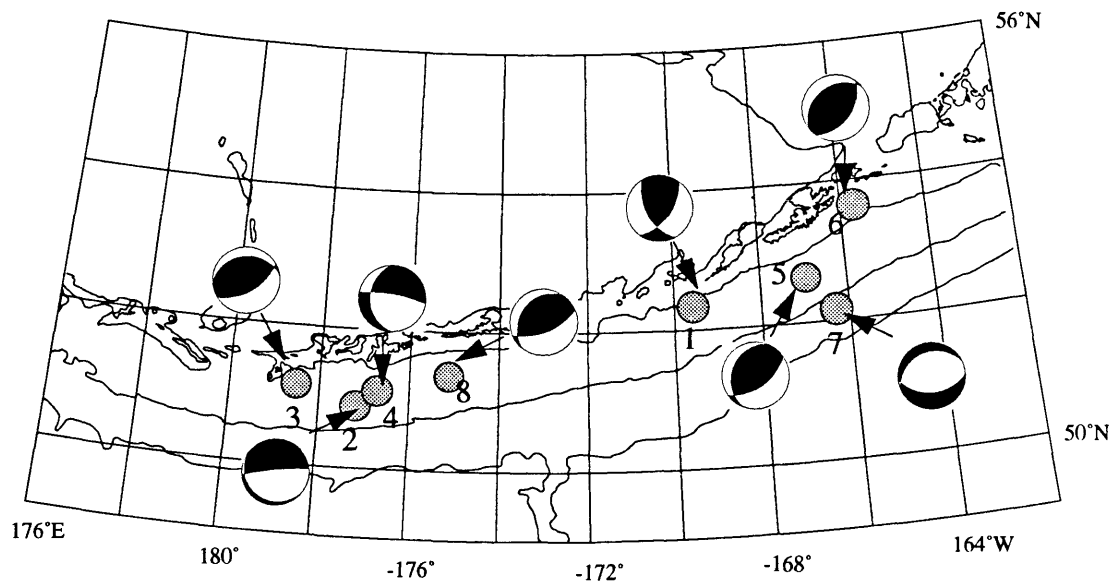


Figure A.1 Epicenter locations and source mechanisms of modeled events. Map is based on an Albert's projection. Source mechanisms are indicated on lower hemisphere, equal area projections with shaded compressional quadrants. Event numbers refer to Table A-1.

Table A.1: Event Locations and Origin Times

Number	Date	Origin Time	Latitude	Longitude
1	March 9,1957	20:39:23.92	52.335	-169.568
2	March 11,1957	03:12:48.86	50.889	-177.182
3	March 11,1957	14:55:26.42	51.156	-178.519
4	March 14,1957	14:47:52.09	51.122	-176.708
5	March 15,1957	02:52:16.35	52.652	-166.937
6	March 22,1957	14:21:13.93	53.624	-165.686
7	April 19,1957	22:19:35.48	52.160	-166.305
8	June 13,1957	10:40:46.03	51.366	-175.129

Event 1 March 9, 1957 (20:39:23.92 GMT)**Solution and errors.**

STRIKE= 150.00°

DIP= 57.00°

SLIP= 35.00°

CENTROID DEPTH= 32.00 +- 3 km

MOMENT= 1.89E+27 +- 1.16E+26 dyne*cm

TIME FUNCTION ELEMENTS (3.00 SEC DURATION):

.347 +- .046

.653 +- .040

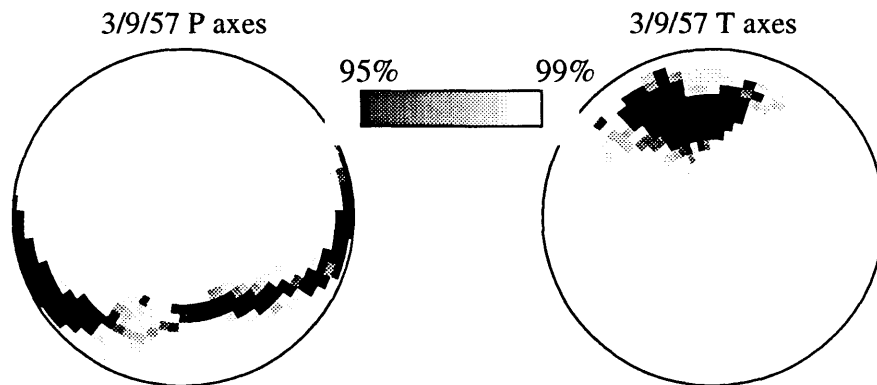


Figure A.2: *P* and *T* axes error surfaces for the earthquake of 3/9/57 (20:39:23.92 GMT). Symbols are as described in Figure 3.10.

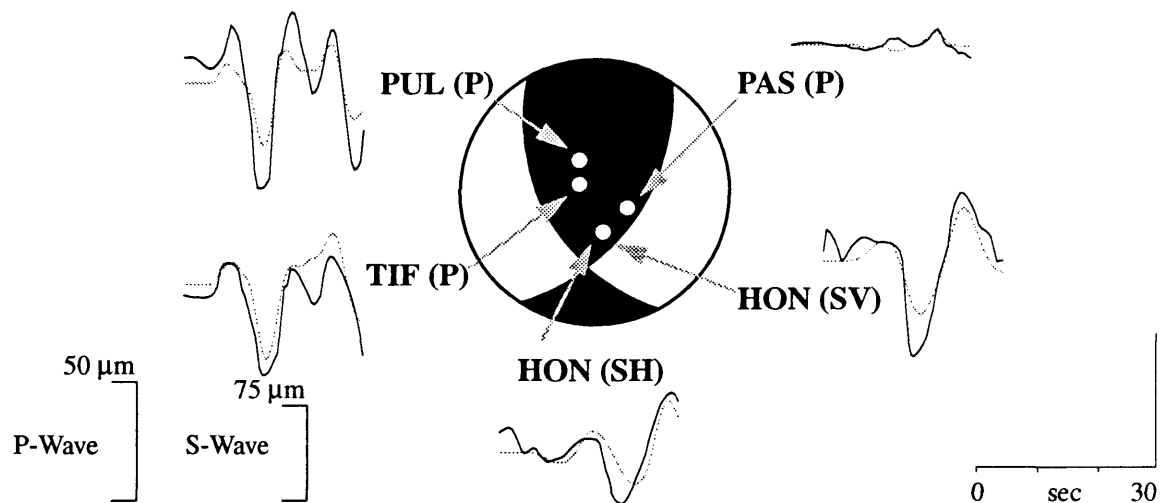


Figure A.3: Waveform solutions for for the earthquake of 3/9/57 (20:39:23.92 GMT). Location of station recording the S-waves (HON) is shown for reference.

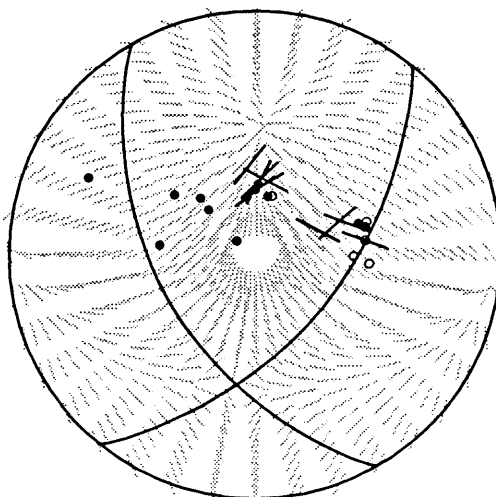


Figure A.4: First motion and S-wave polarization data for for the earthquake of 3/9/57 (20:39:23.92 GMT).

Event 2 March 11,1957 (3:12:48.86 GMT)**Solution and errors.**

STRIKE= 72.00°

DIP= 5.00°

SLIP= -95.00°

CENTROID DEPTH= 34.00 +- 3 km

MOMENT= 3.00E+26 +- 6.32E+25 dyne*cm

TIME FUNCTION ELEMENTS (2.50 SEC DURATION):

1.000 +- .122

.000 +- .136

.000 +- .104

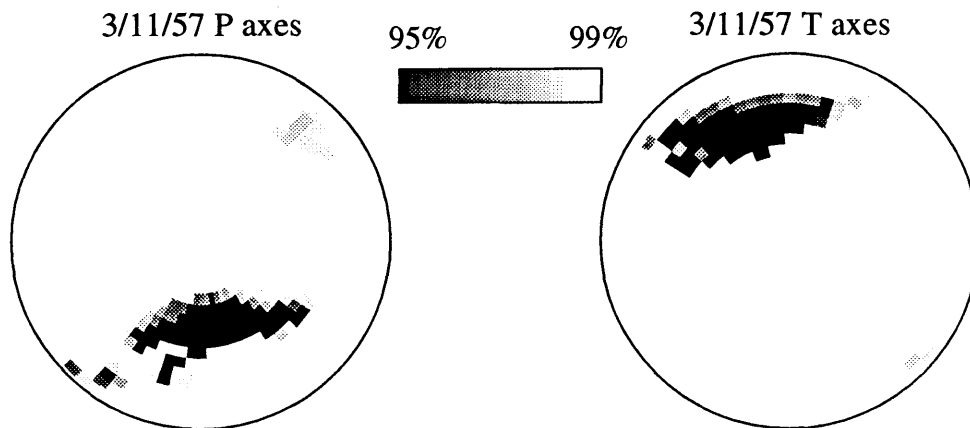


Figure A.5: *P* and *T* axes error surfaces for the earthquake of 3/11/57 (3:12:48.86 GMT). Symbols are as described in Figure 3.10.

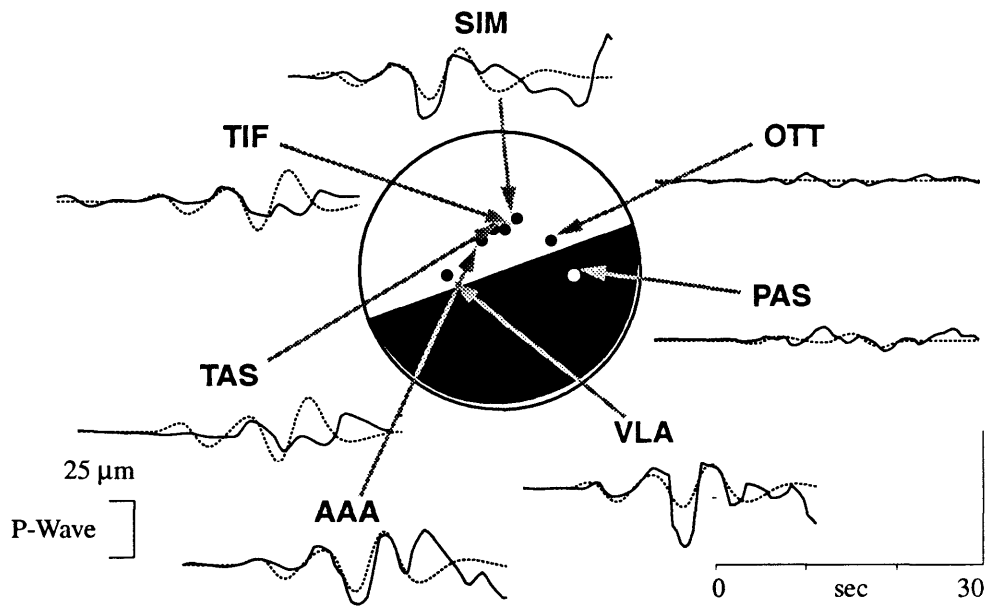


Figure A.6: P-wave seismograms for the earthquake of 3/11/57 (3:12:48.86 GMT)

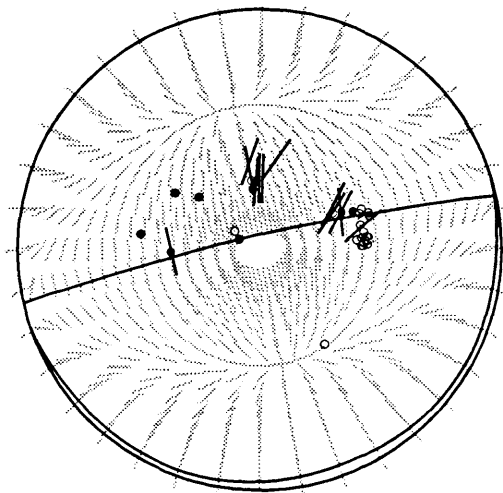


Figure A.7: First motion and S-wave polarization data for the earthquake of 3/11/57 (3:12:48.86 GMT)

Event 3 March 11, 1957 (14:55:26.42 GMT)**Solution and errors.**STRIKE= $264^{\circ} \pm 10^{\circ}$ DIP= $29^{\circ} \pm 4^{\circ}$ SLIP= $118^{\circ} \pm 14^{\circ}$ CENTROID DEPTH= 33 ± 3 kmMOMENT= $2.82E+27 \pm 2.04E+26$ dyne*cm

TIME FUNCTION ELEMENTS (3.00 SEC DURATION):

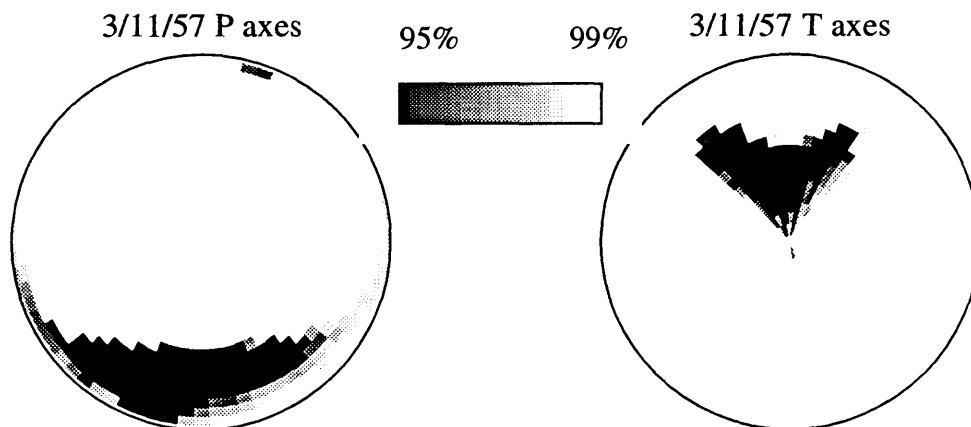
.481 \pm .051.519 \pm .051

Figure A.8: *P* and *T* axes error surfaces for the earthquake of 3/11/57 (14:55:26.42 GMT).

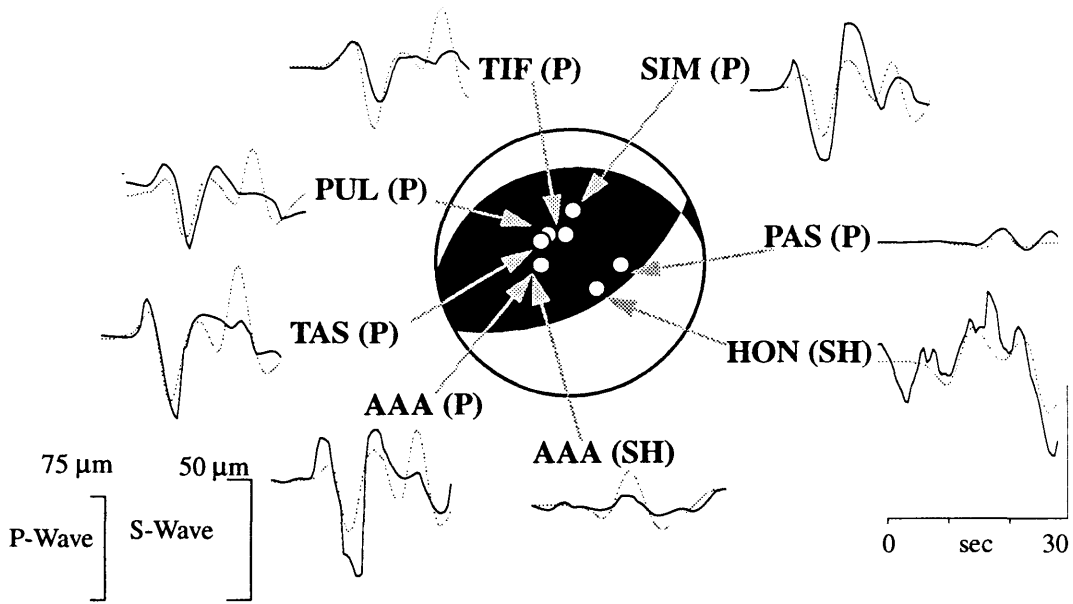


Figure A.9: Waveform solutions for the earthquake of 3/11/57 (14:55:26.42 GMT)

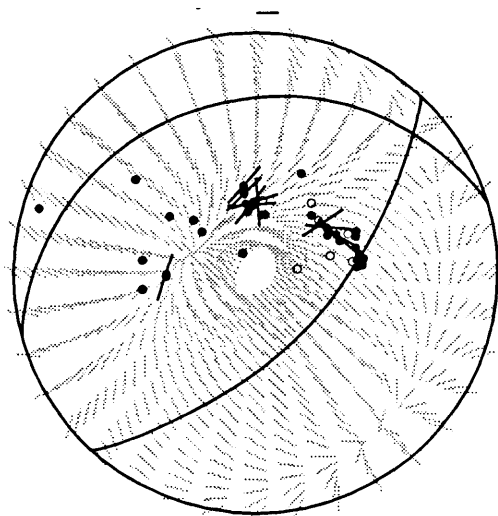


Figure A.10: First motion and S-wave polarization data for the earthquake of 3/11/57 (14:55:26.42 GMT)

Event 4 March 14, 1957 (14:47:52.09 GMT)**Solution and errors.**STRIKE= 180° DIP= 35° SLIP= -15°

CENTROID DEPTH= 33 +- 3 km

MOMENT= $1.96\text{E}+27$ +- $1.26\text{E}+26$ dyne*cm

TIME FUNCTION ELEMENTS (3.00 SEC DURATION):

.594 +- .035

.406 +- .054

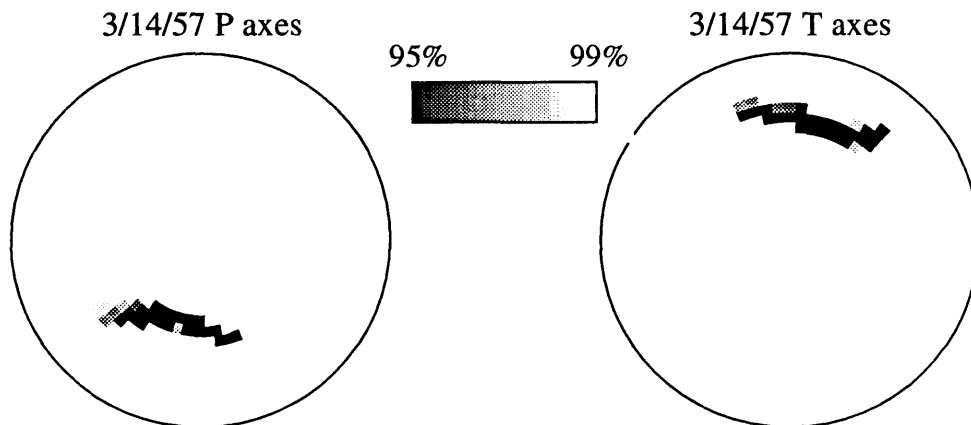


Figure A.11: *P* and *T* axes error surfaces for the earthquake of 3/14/57 (14:47:52.09 GMT)

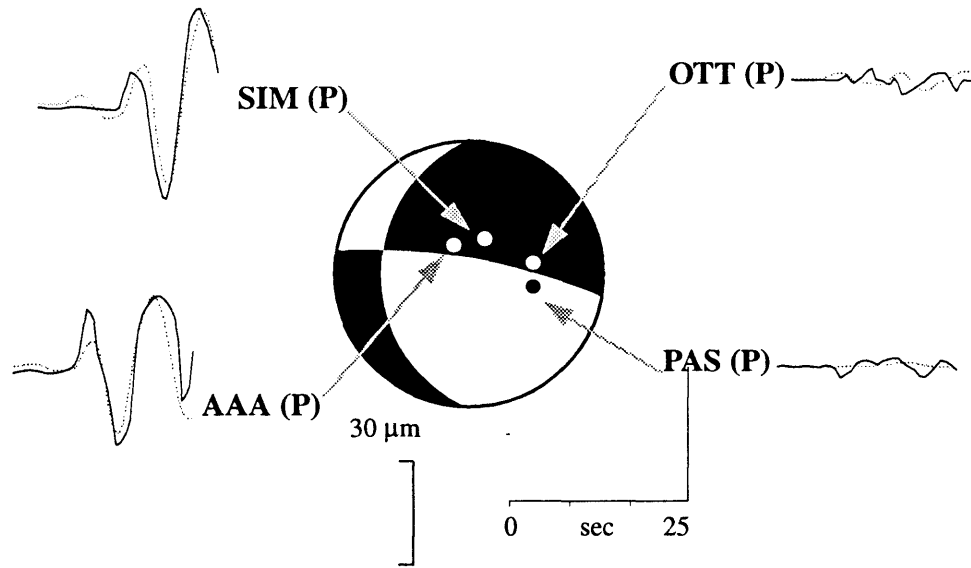


Figure A.12: Waveform solutions for the earthquake of 3/14/57 (14:47:52.09 GMT)

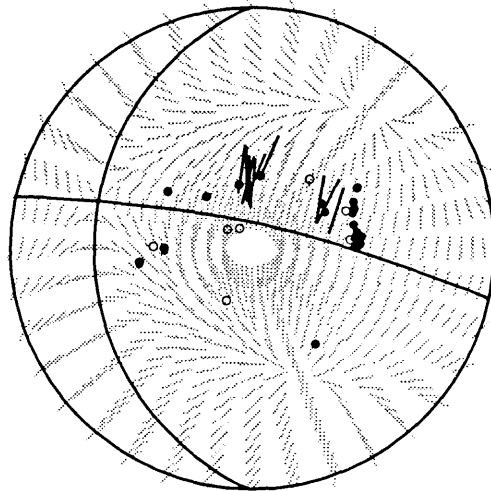


Figure A.13: First motion and S-wave polarization data for the earthquake of 3/14/57 (14:47:52.09 GMT)

Event 5 March 15, 1957 (2:52:16.35 GMT)**Solution and errors.**

STRIKE= 200°

DIP= 30°

SLIP= 60°

CENTROID DEPTH= 17 +- 2 km

MOMENT= 2.07E+26 +- 2.26E+25 dyne*cm

TIME FUNCTION ELEMENTS (1.00 SEC DURATION):

.296 +- .059

.215 +- .070

.489 +- .060

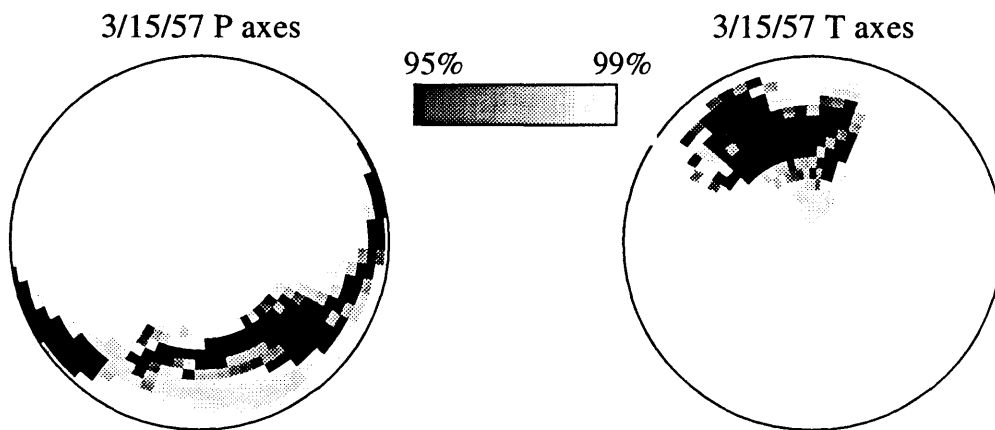


Figure A.14: *P* and *T* axes error surfaces for the earthquake of 3/15/57 (2:52:16.35 GMT)

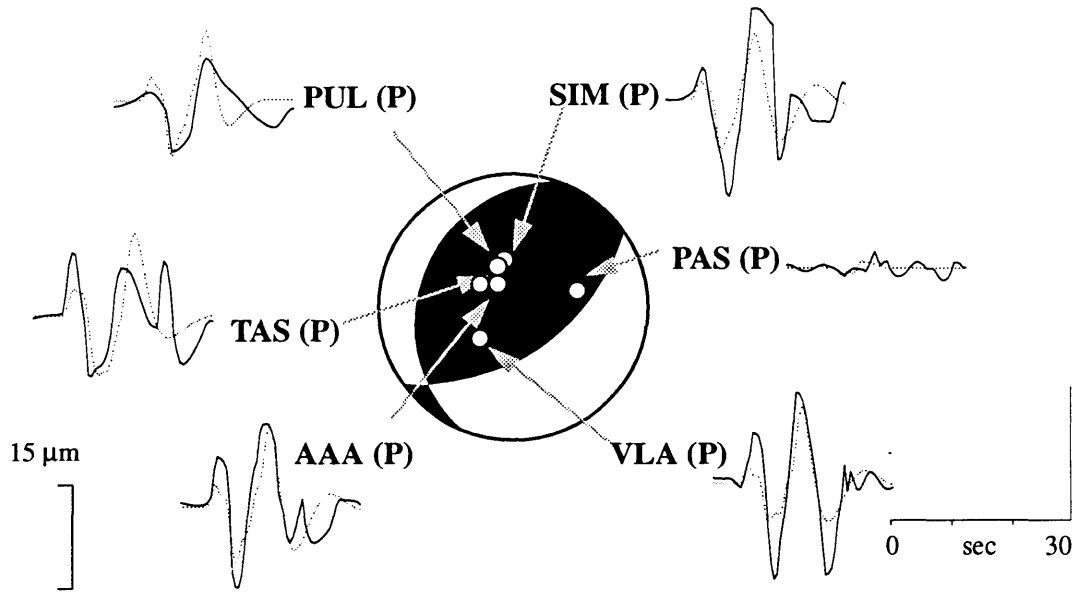


Figure A.15: Waveform solutions for the earthquake of 3/15/57 (2:52:16.35 GMT)

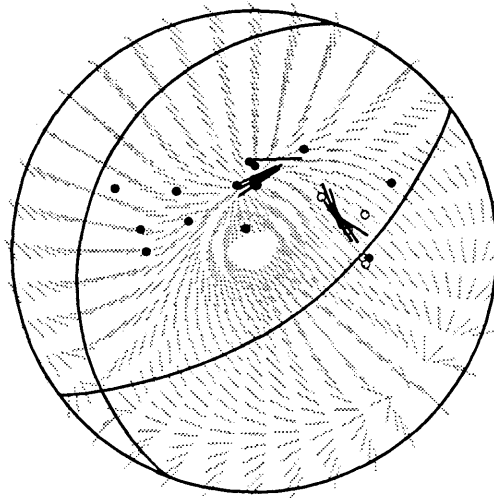


Figure A.16: First motion and S-wave polarization data for the earthquake of 3/15/57 (2:52:16.35 GMT)

Event 6 March 22,1957 (14:21:13.93 GMT)**Solution and errors.**STRIKE= $230^{\circ} \pm 4^{\circ}$ DIP= $24^{\circ} \pm 4^{\circ}$ SLIP= $96^{\circ} \pm 2^{\circ}$ CENTROID DEPTH= 37 ± 4 kmMOMENT= $3.70\text{E}+27 \pm 1.57\text{E}+26$ dyne*cm

TIME FUNCTION ELEMENTS (4.00 SEC DURATION):

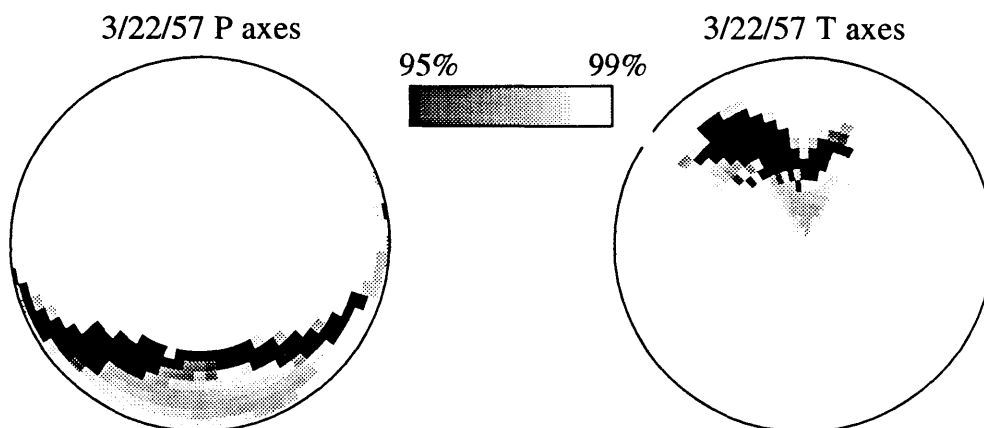
.730 \pm .029.270 \pm .031

Figure A.17: *P* and *T* axes error surfaces for the earthquake of 3/22/57 (14:21:13.93 GMT)

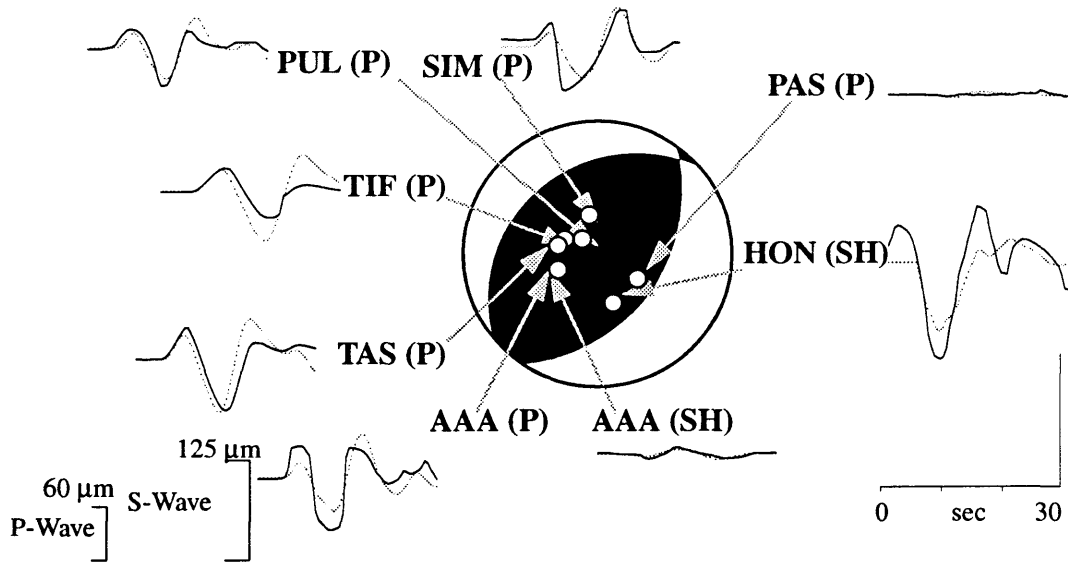


Figure A.18: Waveform solutions for the earthquake of 3/22/57 (14:21:13.93 GMT)

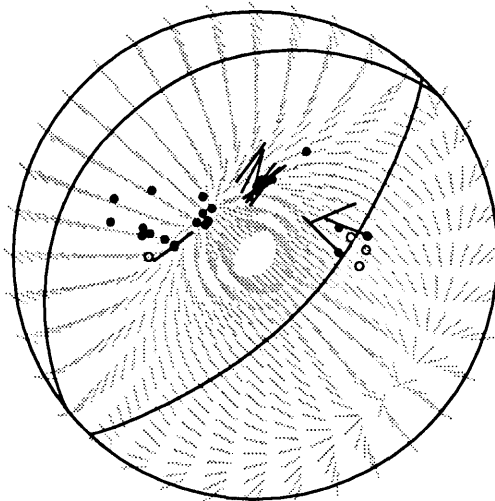


Figure A.19: First motion and S-wave polarization data for the earthquake of 3/22/57 (14:21:13.93 GMT)

Event 7 April 19, 1957 (14:21:13.93 GMT)**Solution and errors.**STRIKE= $245^{\circ} \pm 16^{\circ}$ DIP= $29^{\circ} \pm 4^{\circ}$ SLIP= $-105^{\circ} \pm 13^{\circ}$ CENTROID DEPTH= 12 ± 1 kmMOMENT= $1.69\text{E}+27 \pm 2.30\text{E}+26$ dyne*cm

TIME FUNCTION ELEMENTS (1.00 SEC DURATION):

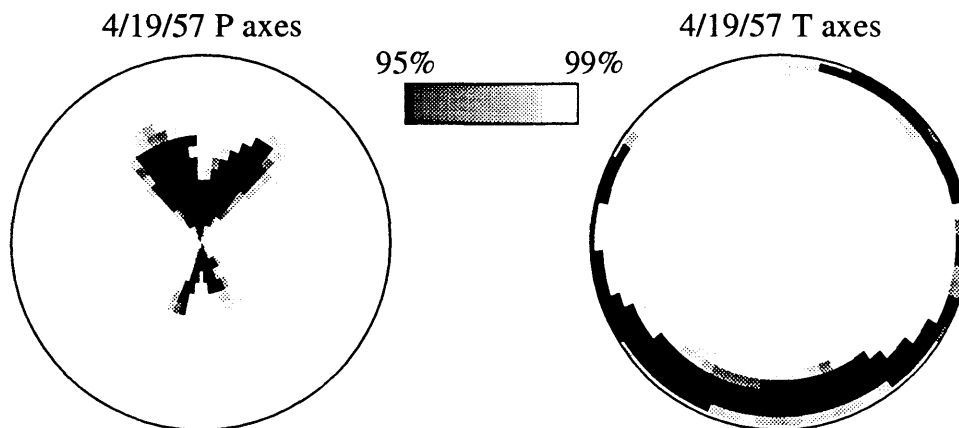
.376 \pm .069.269 \pm .088.356 \pm .077

Figure A.20: *P* and *T* axes error surfaces for the earthquake of 4/19/57 (14:21:13.93 GMT)

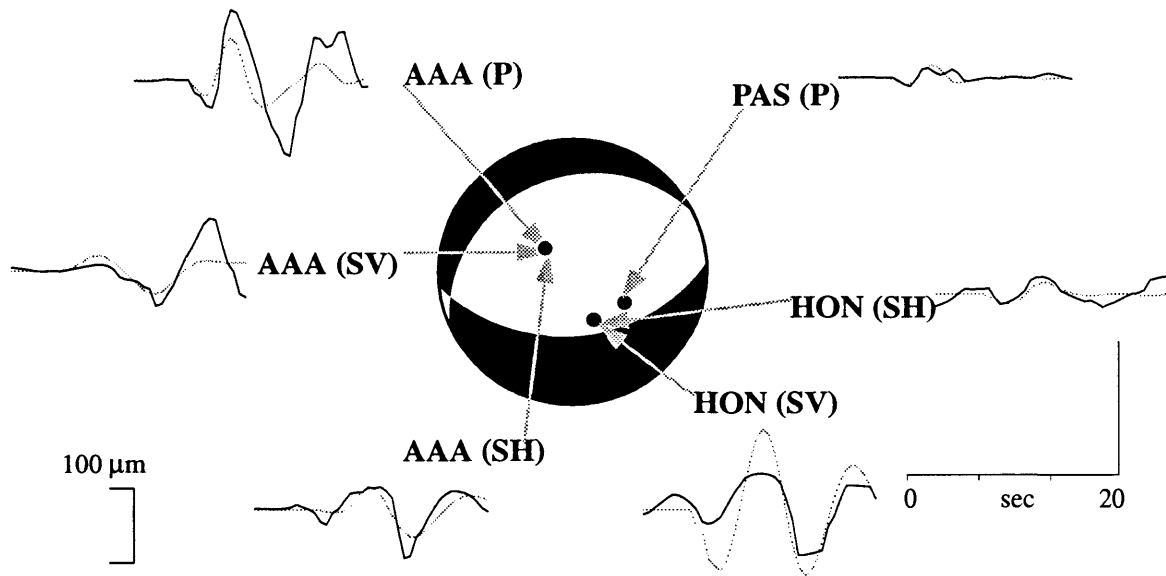


Figure A.21: Waveform solutions for the earthquake of 4/19/57 (14:21:13.93 GMT)

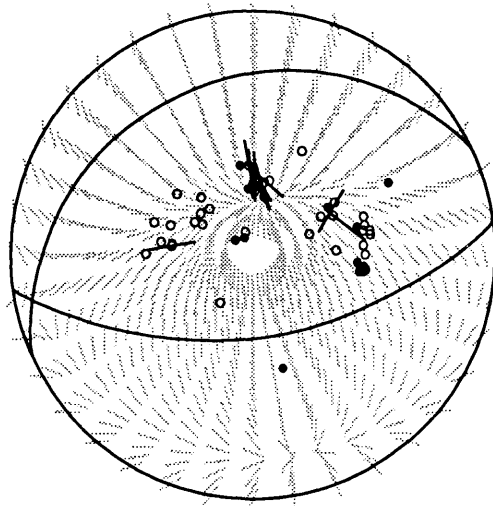


Figure A.22: First motion and S-wave polarization data for the earthquake of 4/19/57 (14:21:13.93 GMT)

Event 8 June 13, 1957 (10:40:46.03 GMT)**Solution and errors.**STRIKE= $67^{\circ} \pm 4^{\circ}$ DIP= $64^{\circ} \pm 6^{\circ}$ SLIP= $108^{\circ} \pm 4^{\circ}$ CENTROID DEPTH= 22 ± 2 kmMOMENT= $1.67\text{E}+27 \pm 7.35\text{E}+25$ dyne*cm

TIME FUNCTION ELEMENTS (3.00 SEC DURATION):

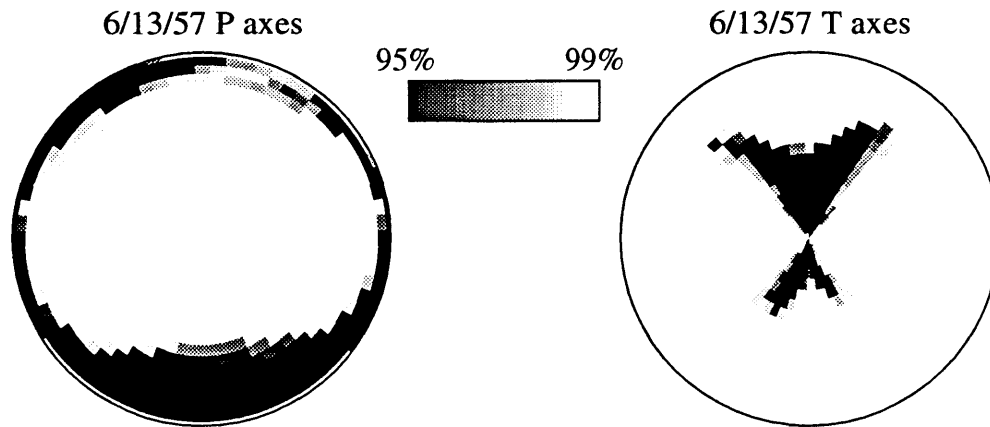
.515 \pm .025.177 \pm .021.308 \pm .030

Figure A.23: *P* and *T* axes error surfaces for the earthquake of 6/13/57 (10:40:46.03 GMT)

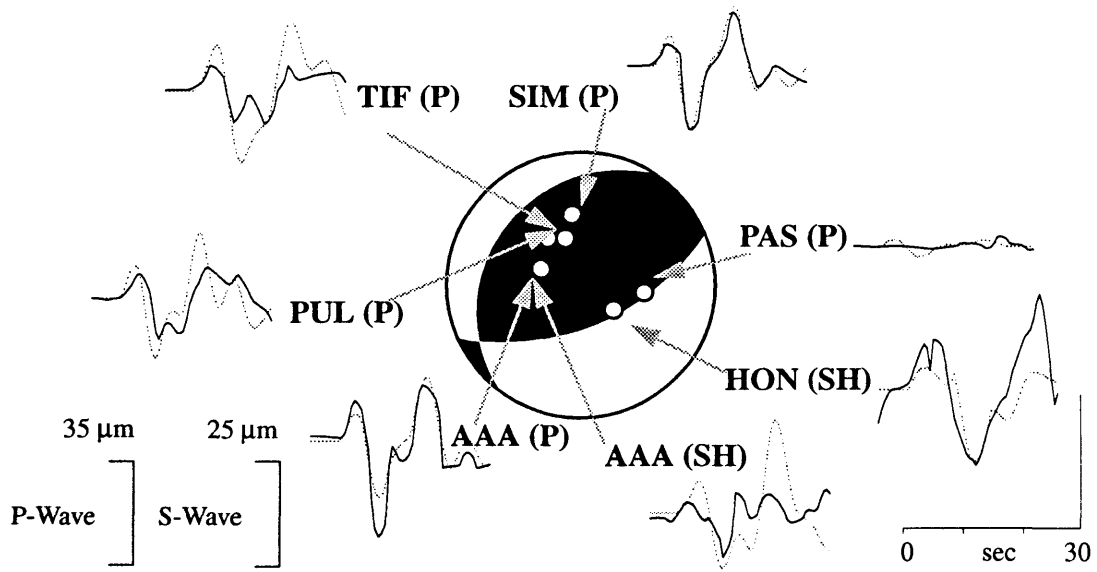


Figure A.24: Waveform solutions for the earthquake of 6/13/57 (10:40:46.03 GMT)

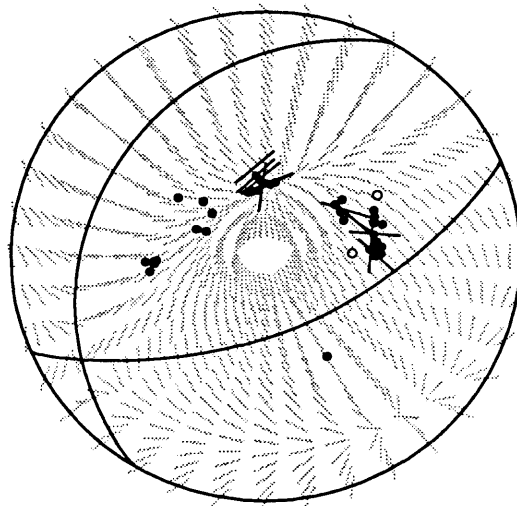


Figure A.25: First motion and S-wave polarization data for the earthquake of 6/13/57 (10:40:46.03 GMT)